International Journal of Heat and Mass Transfer 51 (2008) 6294–6311

Contents lists available at ScienceDirect

International Journal of Heat and Mass Transfer

journal homepage: www.elsevier.com/locate/ijhmt

Analysis of pulsating convection from two heat sources mounted with porous blocks

Po-Chuan Huang *, Chao-Fu Yang

Department of Energy and Refrigerating Air-Conditioning Engineering, National Taipei University of Technology, Taipei 106, Taiwan, ROC

ARTICLE INFO

Article history:
Received 18 July 2006
Received in revised form 5 March 2008
Available online 18 June 2008

Keywords:
Flow pulsating
Darcy–Brinkman–Forchheimer flow model
Periodic steady state

ABSTRACT

The present work details the numerical simulation of forced pulsating convective flow in a parallel-plate channel with two porous-block-attached strip heat sources at the bottom wall. The analysis is based on the use of unsteady Navier–Stokes equation in the fluid region, the transient Darcy–Brinkman–Forchheimer flow model in the porous region, and the energy equation on the thermal field. Both the mixing enhanced convection caused by porous block and the oscillatory enhanced convection caused by pulsation flow are examined. This study details the effects of variations in the Darcy number, pulsating frequency and amplitude, porous blockage ratio, to illustrate important fundamental and practical results. The results show that the periodic alteration in the structure of recirculation flows, caused by both porous block and flow pulsating, has a direct impact on the flow and thermal characteristics near the heat source region. In addition, it is shown that specific choices in certain governing parameters, such as the size or permeability of porous block, and the frequency and amplitude of external pulsation can produce profound enhanced heat transfer on the cooling of heat sources. The cycle-average local surface temperature distribution of heater for pulsating-flow case with porous block is more uniform than that for pure steady-flow case. The method combining flow pulsation with finite-size fiber-porous heat sink can be considered as an augment heat transfer tool for cooling electronic devices.

1. Introduction

The rapid development in the design of electronic packages for modern high-speed computers has led to the demand for new and reliable methods of chip cooling. As stated by Mahalingam and Berg [1], the averaged dissipating heat flux can be up to 25 W/cm^2 for high-speed electronic components. However, the conventional natural or forced convection cooling methods are only capable of removing small heat fluxes per unit temperature difference, about 0.001 W/cm^2 °C by natural convection to air, 0.01 W/cm^2 °C by forced convection to air, and 0.1 W/cm^2 °C by forced convection to liquid [2]. In response to these demands, different highly effective cooling techniques have been used in the past to obtain heat transfer enhancement with a minimum of frictional losses, including a variety of passive or active cooling techniques. Among the heat transfer enhancement schemes, one of the promising techniques is the use of a porous medium subjected to flow pulsation. The porous medium has emerged as an effective passive cooling enhancer due to its large surface area to volume ratio and intense mixing of fluid flow. The forced pulsation of incoming fluid at the entrance of channel is another active augmenting method due to the hydrodynamic instability in a shear layer, which substantially increases lateral, large-scale flow mixing and hence augments the convective thermal transport in the direction normal to the heated surface.

The problem of convective heat transfer in fluid-saturated porous media has been a major topic for various studies during the past decades due to its relevance in a wide range of application such as thermal insulation engineering, water movements, water movements in geothermal reservoirs, nuclear waste repository, heat pipe, grain storage, etc. Extensive studies have been conducted on the steady forced convection flow through a channel fully or partially filled with a porous material as a heat sink for heat transfer augmentation. Koh and Colony [3] analyzed the cooling effectiveness for a porous material in a cooling passage. Kaviany [4] dealt with convective heat transfer from a steady laminar flow through a porous channel bounded by two isothermal parallel plates. Huang and Vafai [5] simulated steady forced convection problem in an isothermal parallel-plate channel with porous-block array. Angirasa [6] numerical reported forced convection in a channel filled with metallic fibrous materials. Their results showed that porous substrate substantially enhance the thermal performance in a channel. Recently, the forced convection heat transfer in a fully/partially porous channel with discrete heated sources or blocks was of special interest due to its applications on the microelectronic cooling. Hadim and Bethancourt [7] investigated forced convection in fully/partially porous channel containing discrete heat sources on the bottom wall. A significant increase in heat transfer rate was observed, as the Darcy number was decrease,

* Corresponding author. Tel.: +886 2 2771 2171x3514; fax: +886 2 2731 4919.
E-mail address: pchuang@ntut.edu.tw (P.-C. Huang).

0017-9310/$ - see front matter © 2008 Elsevier Ltd. All rights reserved.
doi:10.1016/j.ijheatmasstransfer.2008.04.044

Nomenclature

A	oscillating amplitude of axial inlet velocity
C_p	specific heat at constant pressure (J/kg K)
Da	Darcy number, K/R^2
f	dimensional forcing frequency (Hz)
F	function used in expressing inertia terms
h	convective heat transfer coefficient (W/m^2 K)
H_p	height of porous block (m)
J	unit vector oriented along the pore velocity vector, $V_P/\|V_P\|$
k	thermal conductivity (W/m K)
K	permeability of the porous medium (m^2)
L_i	length of channel upstream from the first porous block (m)
L_o	length of channel downstream from the second porous block (m)
L_t	total length of channel (m)
Nu_m	cycle-space average Nusselt number, Eq. (22)
Nu_x	cycle-averaged local Nusselt number, Eq. (21)
$Nu_{x,t}$	local instantaneous Nusselt number, Eq. (20)
P	pressure (N/m^2)
Pe	Pelect number, u_oR/α
Pr	Prandtl number, ν/α
q''	uniform heat flux from each heat source (W/m^2)
R	height of channel (m)
Rc	heat capacity ratio, $(\rho C_p)/(\rho C_p)_f$
Rc_{eff}	effective heat capacity ratio, $(\rho C_p)_{eff}/(\rho C_p)_f$
Re	Reynolds number, u_oR/ν
S	spacing between heat sources or porous blocks (m)
St	dimensionless pulsating frequency, Strouhal number, fR/u_o
t	time (s)
T	temperature (K)
T_x^*	dimensionless cycle-average local temperature
u_o	cycle-averaged velocity of the inlet flow (m/s)
u_i	inlet pulsating velocity (m/s)
u	x-component velocity (m/s)
v	y-component velocity (m/s)
V	velocity vector (m/s)
W	width of heat source or porous block (m)
x, y	Cartesian coordinates (m)

Greek symbols

α	thermal diffusivity (m^2/s)
α_{eff}	effective thermal diffusivity, $k_{eff}/\rho_f c_{p,f}$ (m^2/s)
δ	boundary layer thickness (m)
ε	porosity of the porous medium
λ_{eff}	effective thermal conductivity ratio, k_{eff}/k_f
μ	dynamic viscosity (kg/ms)
ν	kinematic viscosity (m^2/s)
ξ	vorticity (1/s)
ρ	density (kg/m^3)
τ	oscillatory period for a cycle
φ	stream function (m^2/s)
ω	angular velocity (1/s)

Superscript

*	dimensionless quantity

Subscripts

eff	effective
f	fluid
i	inlet
p	porous
s	nonpulsating component
x	local

Symbol

$\langle\rangle$	volume-averaged quantity

especially at the leading edge of each heat source. Angirasa and Peterson [8] numerically studied forced convection heat transfer augmentation in a channel with a localized heat source using metal fibrous material. They concluded that thinner fibers and high porosity media enhance heat transfer because of better distribution flow and mixing. Fu et al. [9] investigated heat transfer from a spherical-bead porous-block-mounted heated wall in a channel flow. They reported that for the blocked ratio $H_p^* = 0.5$ the thermal performances are enhanced by higher porosity and porous particle diameter. However, the result is opposite for $H_p^* = 1$. Huang et al. [10] analyzed forced convective heat transfer from multiple heated blocks in a channel by porous covers and found that the recirculation caused by porous-covering block will significantly augment the heat transfer rate on both top and right faces of second and subsequent blocks.

More recently, due to the needs of high-performance high-power electronic devices, there has been an increasing demand to achieve higher heat transfer removal from the fully/partially porous channel flow. One of such efforts has been given to exploring the use of porous heat sink subjected to pulsation flow. Here, a pulsating channel flow, i.e. an oscillating component superposed on the mean flow in a confined passage, can enhance the axial transfer of energy due to large oscillating temperature gradients in the direction normal to the heated wall. Pulsating flow is frequently encountered in natural system (human respiratory and vascular system) and engineering system (exhaust and intake manifolds of IC engines, regenerator, Stirling engine, etc.). The related characteristics studies on pulsating confined flow heat transfer can be found in Uchida [11], Siegel and Perlmutter [12] and Kim et al. [13]. However, published studies on pulsating convective flow passing through porous channel are scarce. Kim et al. [14] simulated forced pulsating flow in a fully porous channel. The results showed that the effect of pulsation on heat transfer between the channel wall and fluid is more pronounced in case of small pulsating frequency and large pulsating amplitude. Khodadadi [15] analyzed a fully developed oscillatory flow through a porous medium channel bounded by two impermeable parallel plates, showing that the velocity profiles exhibit maxima next to the wall. Paek et al. [16] performed an experimental study of pulsating flow through a porous duct. It was indicated that the heat transport from the porous material decreases as pulsating frequency decreases at given amplitude and is decreased when the pulsating amplitude is large enough to cause a backward flow. Fu et al. [17] conducted experimentally the heat transfer of a porous channel subjected to oscillating flow and found that the length-average Nusselt number for oscillating flow is higher than that for steady flow. Leong and Jin [18] treated experimentally the heat transfer in oscillating flow through a channel filled with an aluminum foam subjected a constant wall heat flux. Their results revealed that the heat transfer in oscillating flow is significantly enhanced by employing porous media in a plate channel. Most of these studies are related to the aspect of forced-pulsation convection over the full-porous system, however, little is known about external forced pulsating convection fluid flow and heat transfer in the

fluid/porous composite system. Guo et al. [19] investigated the pulsating flow and heat transfer in a partially porous pipe and indicated the maximum effective thermal diffusivity was gained by pulsating flow through a pipe partially filled with porous medium rather than the limiting case of no porous medium or the fully filling of porous medium. The purpose of the present study is to explore the effects of both the heat transfer enhancement factors by external flow pulsation and finite-size fiber porous block on the convective cooling of electronic devices.

This paper describes a numerical investigation on flow field and heat transfer characteristics of two successive porous-block-mounted heat sources subjected to pulsating channel flow. Extensive time-dependent flow and temperature data are calculated and averaged over a pulsating cycle in a periodic steady state. The basic interaction phenomena between the porous substrate and the fluid region, as well as the action of pulsation on the transport process are scrutinized within this study. Furthermore, the influences of various parameters governing the hydrodynamic and thermal characteristics of the problem are examined to establish the basic effects and provide practical results. In addition, the results are also compared with those obtained for a steady nonpulsating nonporous-block flow. It is shown that specific choices of descriptive parameters can exert a significant influence in the cooling of the heat source.

2. Analysis and formulation

Consider a pulsating flow in a channel with two discrete heat strip sources, as depicted in Fig. 1a. The channel height and total length are R and L_t, respectively, and both channel walls are insulated. Each heat source dissipates an equal and uniform heat flux q'' over its length W. The porous block, with height H_p and width W_p, mounted on each heat source is used as heat sink. The fluid enters the channel at uniform temperature T_i with a pulsating flow $u_i = u_o[1 + A\sin(\omega t)]$, where A and ω are the pulsating amplitude and frequency, respectively. The flow field is assumed to be unsteady, two-dimensional, single phase, laminar, and incompressible. The fluid properties are constant and the effect of gravity is neglected. Besides, the thermophysical properties of the fluid and the effective properties of the porous medium are assumed to be constant, and the porous medium is considered homogeneous, isotropic, nondeformable, and in local thermal equilibrium with the fluid. Possible channelling near the wall is neglected in the present study because fibrous porous media are considered for which the porosity and permeability are relatively constant even close to the wall [20]. The effective viscosity of porous medium is equal to the viscosity of the fluid.

With the above assumptions, the time-dependent governing conservation equations for the present problem can then be separately written for the porous and fluid regions. Treating the fluid-saturated porous medium as a continuum, the local-volume averages of the conservation equations for mass, momentum, and energy in the porous region are [21]

$$\nabla \cdot \langle V \rangle = 0, \tag{1}$$

$$\left[\frac{1}{\varepsilon}\frac{\partial \langle V \rangle}{\partial t} + \frac{1}{\varepsilon^2}\langle (V \cdot \nabla)V \rangle\right] = -\frac{1}{\rho_f}\nabla \langle p \rangle^f + \left(\frac{\nu_f}{\varepsilon}\right)\nabla^2 \langle V \rangle - \frac{\nu_f}{K}\langle V \rangle - \frac{F}{\sqrt{K}}[\langle V \rangle \cdot \langle V \rangle]J, \tag{2}$$

$$\left\{(\rho C_p)_{\text{eff}}\frac{\partial \langle T \rangle}{\partial t} + (\rho C_p)_f[\langle V \rangle \cdot \nabla \langle T \rangle]\right\} = \nabla \cdot [K_{\text{eff}} \nabla \langle T \rangle]. \tag{3}$$

The transient conservation equations for mass, momentum, and energy in the fluid region are

$$\nabla \cdot V = 0, \tag{4}$$

$$\frac{\partial V}{\partial t} + V \cdot \nabla V = -\frac{1}{\rho_f}\nabla P + \nu_f \nabla^2 V, \tag{5}$$

$$\frac{\partial T}{\partial t} + V \cdot \nabla T = \alpha_f \nabla^2 T. \tag{6}$$

The associated initial and boundary conditions necessary to complete the formulation of the problem are as follows. The unidirectional, pulsating flow at the channel inlet is given

$$\begin{aligned} &x = 0 \quad \text{and} \quad 0 < y < R \quad \text{for } t > 0, \\ &u_i = u_0[1 + A\sin(2\pi f t)], \quad v = 0,\ T = T_i \end{aligned} \tag{7}$$

At the exit, the fully developed conditions are satisfied

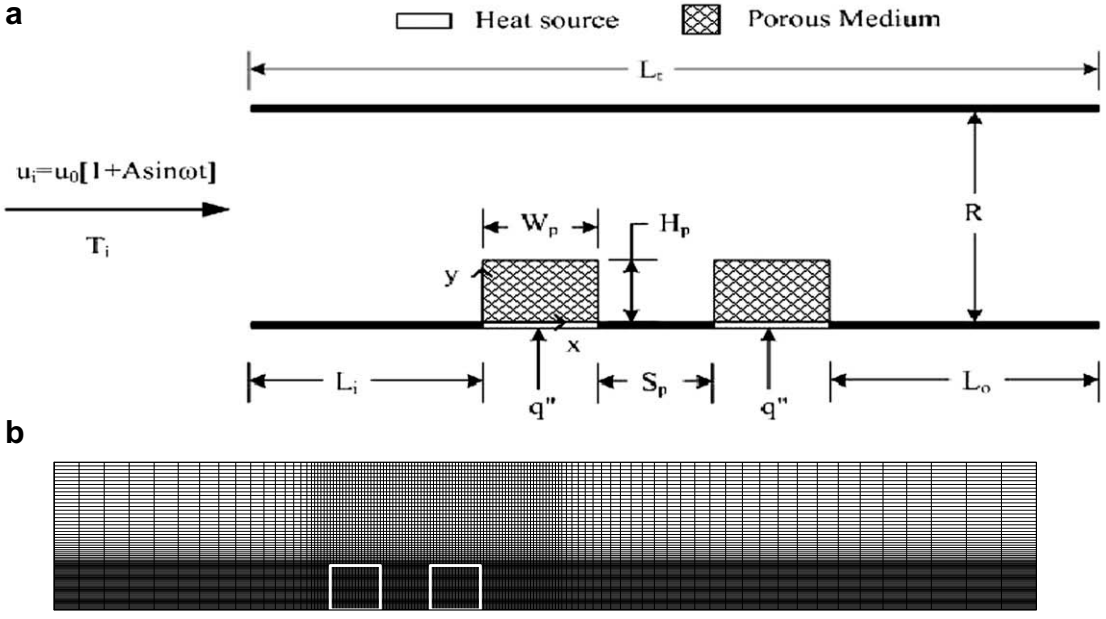

Fig. 1. (a) Schematic diagram of the problem and the corresponding coordinate systems and (b) a typical nonuniform grid system for the whole computational domain.

$$\frac{\partial u}{\partial x}=0,\quad \frac{\partial v}{\partial x}=0,\quad \frac{\partial T}{\partial x}=0 \quad \text{for } x=L_t \text{ and } 0<y<R \text{ for } t>0 \tag{8}$$

The no-slip conditions at the perfect-insulated channel walls are

$$u=0,\quad v=0,\quad \frac{\partial T}{\partial y}=0 \quad \text{at } \begin{cases} 0<x<L_i \text{ and } y=R \\ x<L_t \text{ and } L_i+W_p<x<L_t,\ y=0 \end{cases} \quad \text{for } t>0. \tag{9}$$

At the wall of heat sources $L_i<x<L_i+W_p$, and $L_i+W_p+S_p<x<L_t-L_0$, $y=0$, for $t>0$

$$u=0,\quad v=0,\quad \frac{\partial T}{\partial y}=-\frac{q''}{k_f}. \tag{10}$$

Along the fluid/porous interface, the continuities of the velocity, pressure, stress, temperature, and heat flux are satisfied [5].

Introducing the stream function φ and vorticity ζ as

$$u=\langle u\rangle=\frac{\partial \varphi}{\partial y},\quad v=\langle v\rangle=-\frac{\partial \varphi}{\partial x},\quad \zeta=\frac{\partial v}{\partial x}-\frac{\partial u}{\partial y}=\frac{\partial\langle v\rangle}{\partial x}-\frac{\partial\langle u\rangle}{\partial y} \tag{11}$$

and the following dimensionless variables:

$$x^*=x/R,\quad y^*=y/R,\quad u^*=u/u_o,\quad v^*=v/u_o,$$
$$W_p^*=W_p/R,\quad H_p^*=H_p/R \tag{12a}$$
$$St=fR/u_o,\quad T^*=(T-T_i)/(q''R/k_f),\quad t^*=tu_o/R,$$
$$\varphi^*=\varphi/u_iR,\quad \zeta^*=R\zeta/u_i. \tag{12b}$$

Then the above two sets of conservation equations are transformed into one set of dimensionless stream function-vorticity formulation, which is valid throughout the composite system, as follows:

$$\varepsilon\frac{\partial \zeta^*}{\partial t^*}+u^*\frac{\partial \zeta^*}{\partial x^*}+v^*\frac{\partial \zeta^*}{\partial y^*}=\frac{\varepsilon}{Re}\nabla^2\zeta^*+S_\varphi^*, \tag{13}$$

$$\nabla^2\varphi^*=-\zeta^*, \tag{14}$$

$$Rc\frac{\partial T^*}{\partial t^*}+u^*\frac{\partial T^*}{\partial x^*}+v^*\frac{\partial T^*}{\partial y^*}=\nabla\cdot\left(\frac{\lambda}{Pe}\nabla T^*\right). \tag{15}$$

The dimensionless parameters in Eqs. (13)–(15) are Reynolds number Re, the heat capacity ratio Rc, the thermal conductivity ratio λ, and the Pelect number Pe. S_φ^* is the source term. Then, the dimensionless parameters in the fluid region are

$$Rc_f=(\rho C_p)_f/(\rho C_p)_f=1,\quad Re_f=u_oR/\nu_f,\quad Pe_f=u_oR/\alpha_f,\quad \lambda_f=k_f/k_f=1,\quad S_\varphi^*=0,\quad \varepsilon=1. \tag{16}$$

And in the porous region the dimensionless parameters are

$$Rc_{eff}=(\rho C_p)_{eff}/(\rho C_p)_f,\quad Re_{eff}=u_oR/\nu_{eff},$$
$$Pe_{eff}=u_oR/\alpha_{eff},\quad \lambda_{eff}=k_{eff}/k_f, \tag{17a}$$

$$S_\varphi^*=-\frac{\varepsilon^2}{Re_{eff}Da}\zeta^*-\frac{F\varepsilon^2}{\sqrt{Da}}|\vec{V}^*|\zeta^*-\frac{F\varepsilon^2}{\sqrt{Da}}\left[v^*\frac{\partial|\vec{V}^*|}{\partial x^*}-u^*\frac{\partial|\vec{V}^*|}{\partial y^*}\right], \tag{17b}$$

where the Darcy number, $Da=K/R^2$, is related to the permeability of the porous medium. ε denotes the porosity, F the inertia coefficient of porous medium, and k_{eff} the effective thermal conductivity of fluid-saturated porous medium.

The corresponding dimensionless boundary conditions thus become:

$$u^*=1+A\sin(2\pi Stt^*),\quad v^*=0,\quad T^*=0,\quad \varphi^*=y^*,\quad \zeta^*=0 \quad \text{at } x^*=0,\quad 0<y^*<1,\quad t^*>0, \tag{18a}$$

$$\frac{\partial \varphi^*}{\partial x^*}=0,\quad \frac{\partial \zeta^*}{\partial x^*}=0,\quad \frac{\partial T^*}{\partial y^*}=0 \quad \text{at } x^*=L_t^*,\quad 0<y^*<1,\quad t^*>0 \tag{18b}$$

$$u^*=0,\quad v^*=0,\quad \varphi^*=0,\quad \zeta^*=-\frac{\partial^2\varphi^*}{\partial y^{*2}},$$
$$\frac{\partial T^*}{\partial y^*}=\begin{cases}0 & \text{(at insulated area)}\\ -1/\lambda_{eff} & \text{(at heat source area)}\end{cases} \quad \text{at } 0<x^*<L_t^*,\quad y^*=0,\quad t^*>0, \tag{18c}$$

$$\varphi^*=1,\quad \zeta^*=-\frac{\partial^2\varphi^*}{\partial y^{*2}},\quad \frac{\partial T^*}{\partial y^*}=0,\quad u^*=0,\quad v^*=0 \quad \text{at } 0<x^*<L_t^*,\quad y^*=1,\quad t^*>0, \tag{18d}$$

where $St=fR/u_o$ is the dimensionless pulsating frequency parameter (Strouhal number), and along the fluid/porous interface

$$u_p^*|_{g(x,y)=0}=u_f^*|_{g(x,y)=0},\quad v_p^*|_{g(x,y)=0}=v_f^*|_{g(x,y)=0},$$
$$\mu_{eff}\left.\frac{\partial v_p^*}{\partial n^*}\right|_{g(x,y)=0}=\mu_f\left.\frac{\partial v_f^*}{\partial n^*}\right|_{g(x,y)=0}, \tag{19a}$$

$$\mu_{eff}\left.\left[\frac{\partial u_p^*}{\partial n^*}+\frac{\partial v_p^*}{\partial t^*}\right]\right|_{g(x,y)=0}=\mu_f\left.\left[\frac{\partial u_f^*}{\partial n^*}+\frac{\partial v_f^*}{\partial t^*}\right]\right|_{g(x,y)=0}, \tag{19b}$$

$$T_p^*|_{g(x,y)=0}=T_f^*|_{g(x,y)=0},$$
$$k_{eff}\left.\frac{\partial T_p^*}{\partial n^*}\right|_{g(x,y)=0}=k_f\left.\frac{\partial T_f^*}{\partial n^*}\right|_{g(x,y)=0}. \tag{19c}$$

For further insight into the effects of both flow pulsation and porous block on the heat transfer rate at the heat source, the local instantaneous Nusselt number along the surfaces of the heat sources is evaluated as

$$Nu_{x,t}=\frac{h(x,t)R}{k_f}=-\frac{k_{eff}R}{k_f(T_w-T_o)}\left.\frac{\partial T_{x,t}}{\partial y}\right|_{y=0}=-\frac{k_{eff}}{k_fT_w^*}\left.\frac{\partial T^*_{x^*,t^*}}{\partial y^*}\right|_{y^*=0}, \tag{20}$$

where $T_w^*=(T_w-T_i)/(q''R/k_f)$ is the dimensionless heater surface temperature. Then the corresponding local Nusselt number in a time average over one cycle of pulsation is calculated as

$$Nu_x=\frac{1}{\tau}\int_0^\tau Nu_{x,t}\,dt. \tag{21}$$

The cycle-space averaged Nusselt number over a heat source is defined as

$$Nu_m=\frac{1}{\tau W}\int_0^\tau\int_0^w Nu_{x,t}\,dx\,dt, \tag{22}$$

where W is the overall exposed length of heat source. Noted that the definition of Nusselt number based on the conductivity of the fluid permits a direct comparison for a heat source with and without porous block.

3. Numerical method and procedure

To obtain the solution of foregoing system of equations, the region of interest is overlaid with a variable grid system as shown in Fig. 1b. Applying the first-order fully implicit scheme for the time derivatives, the central differencing for the diffusion terms and the second upwind differencing for the convective terms, the transient finite-difference form of the vorticity transport, stream function and the energy equations were derived by control-volume integration of these differential equations over discrete cells surrounding any given grid point. The transient finite-difference equations were solved by the extrapolated-Jacobi scheme. This iterative scheme is based on a double cyclic routine, which translates into a sweep of only half of the grid points at each iteration step [22]. In this work, convergence was considered to have been achieved when the absolute value of relative error on each mesh point between two successive iterations was found to be less than 10^{-6}. In most cases, steady periodic solutions were obtained after 15–45 cycles of

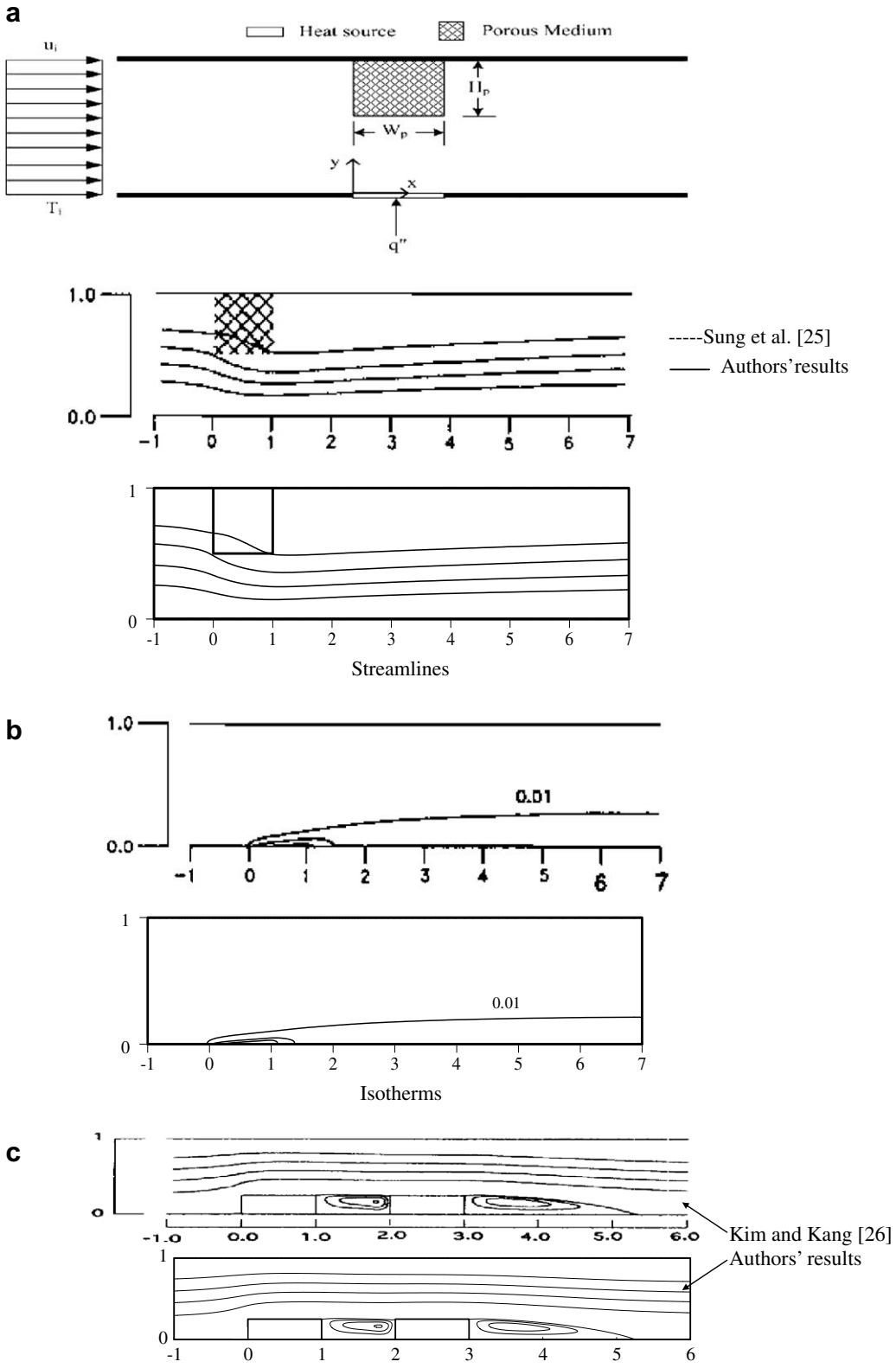

Fig. 2. The results compared with other literatures: (a) and (b) streamlines and isotherms compared with Sung et al. [25], (c) and (d) space-averaged Nusselt number $(Nu_m)_s$ for the steady nonpulsating flow compared with Kim and Kang [26], and (e) and (f) profiles of time-dependent fluctuation of u^* compared with Kim et al. [14] for $St = 0.006$ and 0.16, respectively.

pulsation. The time resolution was such that one pulsating period was divided into 60 time steps during the early 5–10 cycles, and into 120 time steps for later cycles. It should be noted that since the size of time step is related to the frequency, the time step was reduced until a further reduction did not significantly affect the convergent results for different dimensionless pulsating frequency parametric values. The time resolution used in this paper is suitable for all frequencies in the investigating range, $0 < St \leqslant 2$.

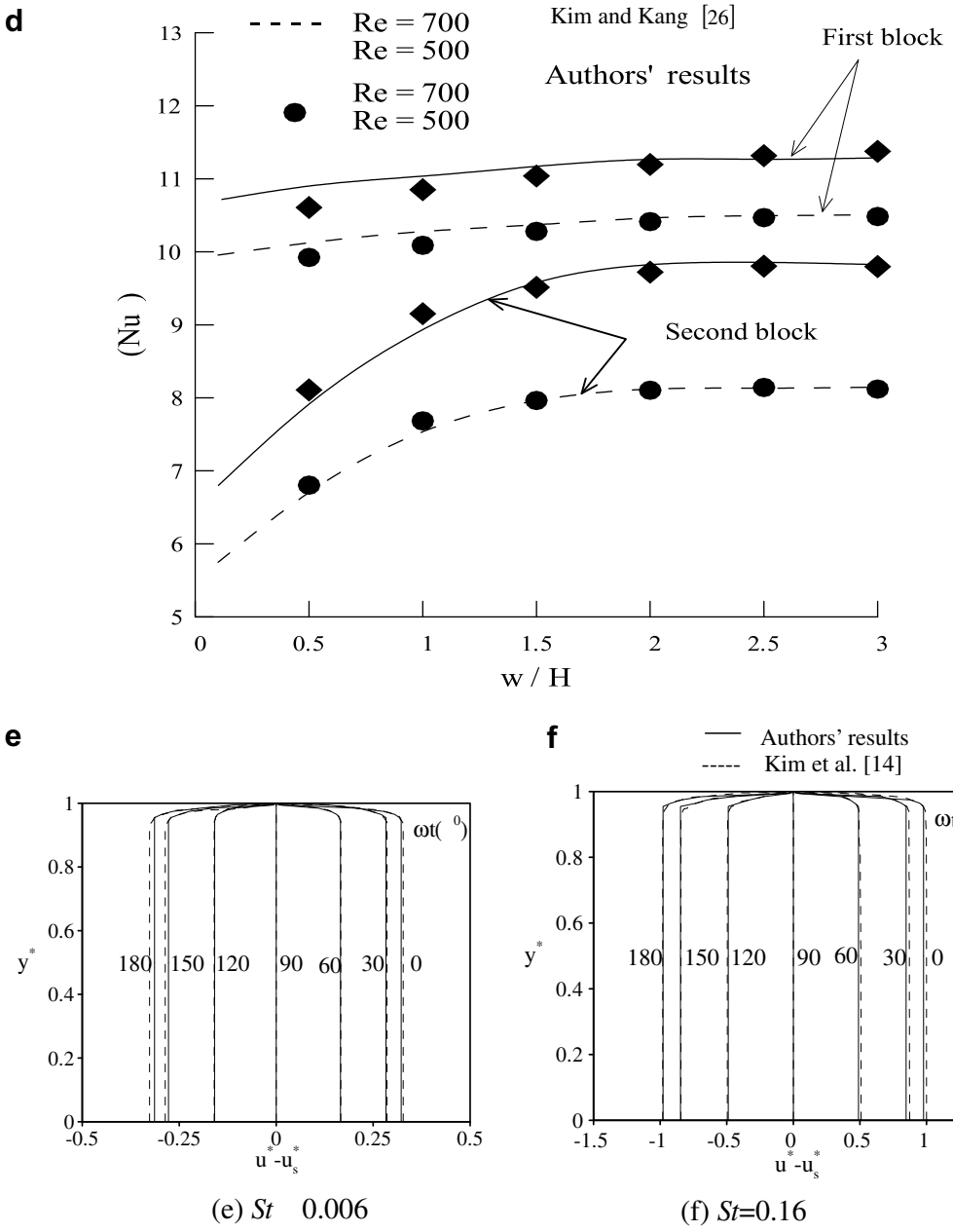

Fig. 2 (*continued*)

In addition, the harmonic mean formulation suggested by Patankar [23] was used to handle abrupt variations in thermophysical properties, such as the permeability, inertia factor, and thermal conductivity, across the interface. This ensures the continuity of the convective and diffusive fluxes across the porous/fluid interface.

A nonuniform spatial grid system, which possesses a very fine grid structure through the porous blocks as well as its immediate surroundings and gradually becomes coarser toward the far field, was employed to obtain accurate vorticity, streamline, and isotherm distribution. Fig. 1b depicts a nonuniform grid system for the computational domain. A grid independence test showed that there is only a very small difference (less than 1%) in the space–time averaged Nusselt number among the solution for (117×77), (127×95), (161×122), (178×143) and (226×161) grid distributions. Therefore, a 178×143 grid system was adopted for the present work. Also, particular attention was given to the spatial mesh points in the boundary layer, since the boundary layer thickness δ/R for the classical oscillatory flow on a flat plate can be estimated as follows [24]:

$$\delta \sim (2\nu/\omega)^{1/2}; \quad \delta/R \sim 1/(StRe)^{1/2}. \tag{23}$$

Thus the dimensionless boundary layer thickness becomes smaller as St and/or Re increases. Spatial grids were clustered to resolve the region of this thin boundary layer for high-frequent pulsation.

The mathematical model and the numerical scheme were checked by comparing the results obtained from the present numerical results with other relevant limiting cases available in the literature. The relevant studies for our case correspond to the problems: (1) a steady forced convection from a isolated heat source in a channel with a porous block attached to the upper surface wall vertically above the heating zone, (i.e., $St = 0$, $H_p^* = 0.5$, $W_p^* = 1.0$ for $Re = 500$, $Da = 1 \times 10^{-2}$, $F = 0.55$, $\varepsilon = 0.9$, $k_{eff}/k_f = 1$, $Pr = 0.72$, $L_i^* = 5.5$, $L_o^* = 15$); (2) a steady nonpulsating forced

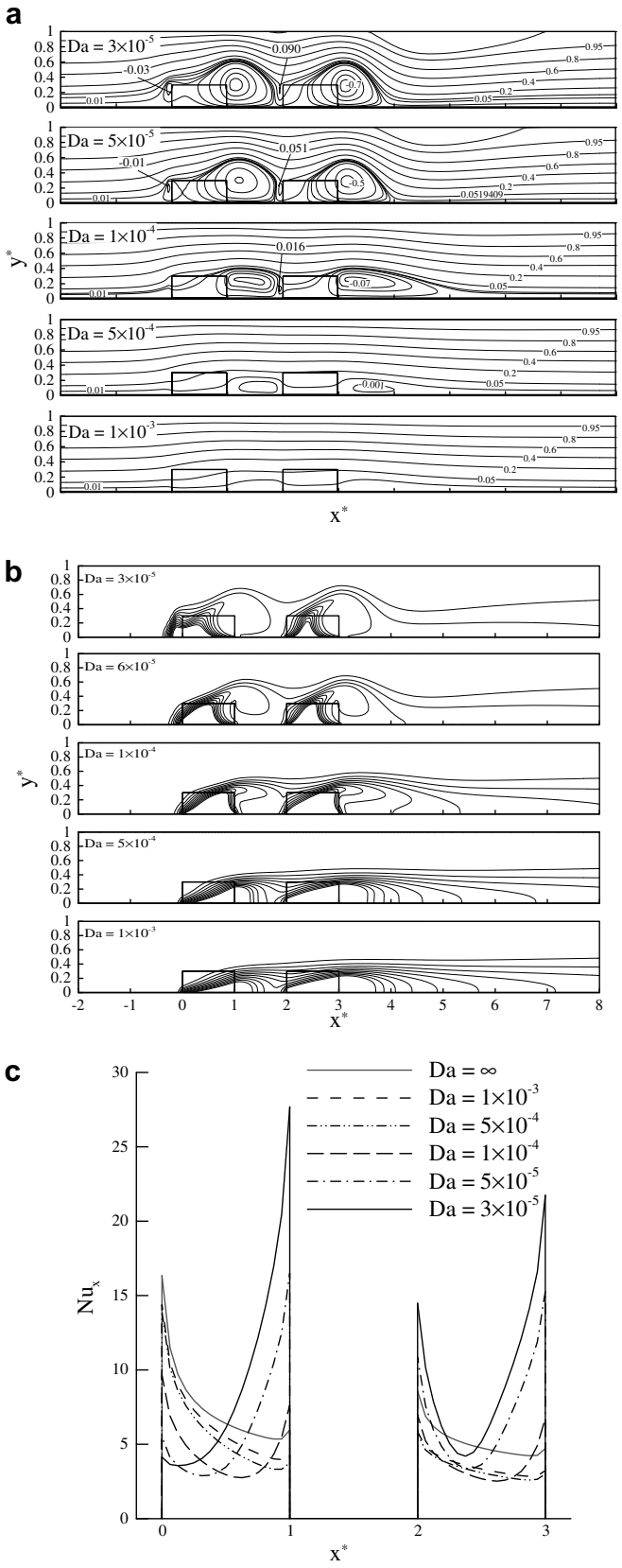

Fig. 3. Effects of the Darcy number on (a) streamlines ($\Delta\varphi^* = 0.2$ for $0 < \varphi^* < 1$) and (b) isotherms ($\Delta T^* = 0.1$ for $0 < \Delta T^* < 1$) (c) local Nusselt number distribution and (d) the heat transfer enhancement factor $Nu_m/(Nu_m)_{\text{non-s}}$for a steady nonpulsating flow.

flow in a channel with two heat solid blocks at uniform temperature, that is, $Da \to 0$, and $St = 0$ for $Pr = 0.7$, $H_s^* = 0.25$, $S_s^* = 1.0$, $k_s/k_f \to \infty$, $L_i^* = 5.0$, $L_o^* = 29.0$ at $Re = 500$ and 700 for $0.5 \leqslant W_s^* \leqslant 3$; (3) a forced pulsating flow in a channel filled with fluid-saturated porous media, that is, $H_p^* = 1$, $W_p^* \to \infty$. The results for the first case are within less than 1% agreement with the data reported by Sung et al. [25] for both streamlines and isotherms, as shown in Fig. 2a and b. For the second case, the results agree to better than 2.1 percent with data provided by Kim and Kang [26] for streamlines and space-averaged Nusselt number $(Nu_m)_s$ of each solid block for the steady nonpulsating channel flow over two heat blocks, as shown in Fig. 2c–d. The third validity was to compare with the study of Kim et al. [14] for $Da = 10^{-4}$, $Re = 50$, $Pr = 0.7$, $F = 0.057$, $\varepsilon = 0.6$, $A = 0.75$, $St = 0.006$ and 0.16. Comparisons between the profiles of normalized time-dependent fluctuation $u_{t-s}^* = u_t^* - u_s^*$ of velocity u^*, where u_t^* is the total instantaneous velocity and u_s^* denotes the nonpulsating steady part, calculated in Kim et al. [14] and the current analysis show discrepancies less than 1.5%, as shown in Fig. 2e and f.

4. Results and discussion

The fixed input parameters that were used for cases were $Pr = 0.7$ (the air is used as the cooling fluid) $L_i^* = 5.0$, $L_o^* = 12$, $W_p^* = 1$, $F = 0.057$, $\varepsilon = 0.6$, $Re = 250$. In this study, emphasis is placed on the effects of Darcy Number $(1 \times 10^{-5} \leqslant Da \leqslant 1 \times 10^{-3})$, pulsation frequency $(0 \leqslant St \leqslant 2)$, the pulsation amplitude $(0.05 \leqslant A \leqslant 0.9)$ and the porous-block aspect ratio $(0.1 \leqslant H_p^* \leqslant 0.4)$ on the flow and heat transfer characteristics. To illustrate the results of flow and temperature fields near the porous-block-mounted strip heat sources clearly, only this region and its vicinity are presented. However, it should be noted that the computational domain included a much larger region than what is displayed in the subsequent figures. Furthermore, for the sake of brevity, only the main features and characteristics of some of the results are discussed and the corresponding figures are not presented.

4.1. Steady flow

For comparison purpose, the typical velocity and temperature fields around the porous-block-mounted heat sources in the case of a steady nonpulsating flow ($St = 0$) are displayed in the Fig. 3 for $Re = 250$, $H_p^* = 0.3$, $W_p^* = 1.0$, $S_p^* = 1.0$, $\lambda_{\text{eff}} = 1$, at $Da = 1 \times 10^{-3}$, 5×10^{-4}, 1×10^{-4}, 5×10^{-5}, and 3×10^{-5}, respectively. As can be seen from Fig. 3 that as Darcy number decreases from 1×10^{-3} to 1×10^{-4}, the streamlines inside the porous blocks move upward and a recirculation zone is gradually formed behind each porous block. When Da is decreased further to 3×10^{-5}, the height of these recirculation regions becomes higher than that of porous block. Besides, these large recirculations behind each porous block are separated by a small vortices rotating in a direction opposite to that of the larger recirculations. At the same time, a relatively smaller vortex is created ahead of the first porous block, and a weak eddy is generated on the smooth upper plate surface corresponding to the flow-reattached region on the bottom plate. The variation of these complicated flowfield within the channel is the consolidated result of the following four effects: (1) a penetrating effect pertaining to the porous medium, (2) a blowing effect caused by porous media displacing transversely the fluid from the porous region into the fluid region, (3) a suction effect caused by the pressure drop behind the porous blocks resulting in a reattached flow, (4) the effects of boundary-layer separation. The interactions of the recirculations, caused by the porous block, with the core flow play a significant role in affecting the temperature field. The temperature field corresponding to the above flow field is

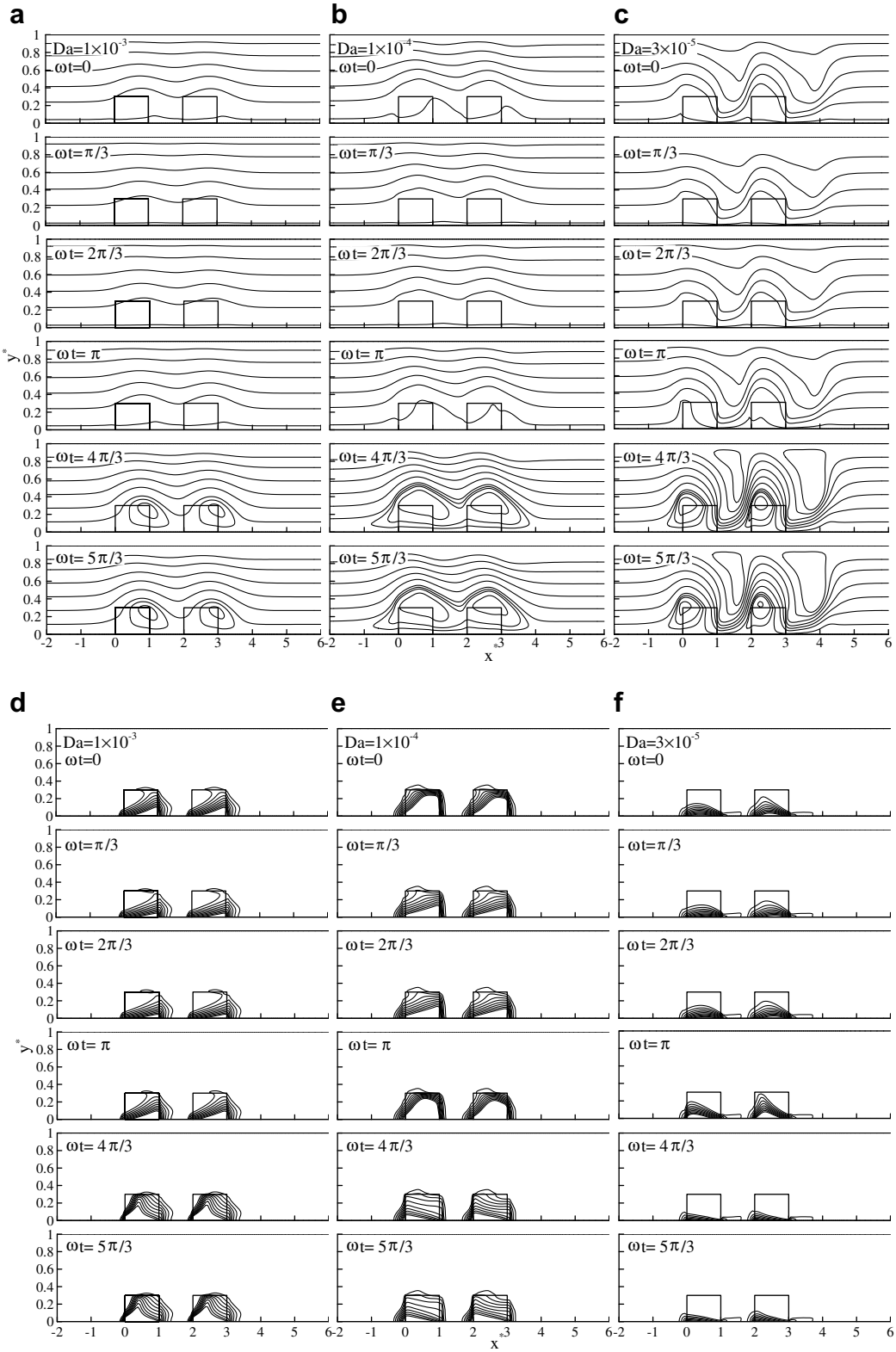

Fig. 4. Effects of the Darcy number on the variations of streamlines ($\Delta\varphi^* = 0.2$ for $0 < \varphi^* < 1$) (a)–(c), isotherms ($\Delta T^* = 0.1$) (d)–(f), cycle-averaged Nusselt number (g), and heat transfer enhancement factor (h) during a periodic-steady cycle.

displayed in Fig. 3b. On the top interface of each porous block the isotherms spread upward duo to the blowing effect, while on the rear interfacial surface the isotherms are crowded upwind due to the neighboring clockwise-rotating recirculation effect. The extent of distortion for entire isotherms become more pronounced as Darcy number decreases from 1×10^{-3} to 3×10^{-5}. The relationship between Nu_x and Da is shown in Fig. 3c. For the case of steady nonpulsating flow ($St = 0$) without porous block ($Da \to \infty$), a large Nusselt number Nu_x occurs at the leading edge of each heat source where the thermal boundary layer begins to grow, and then

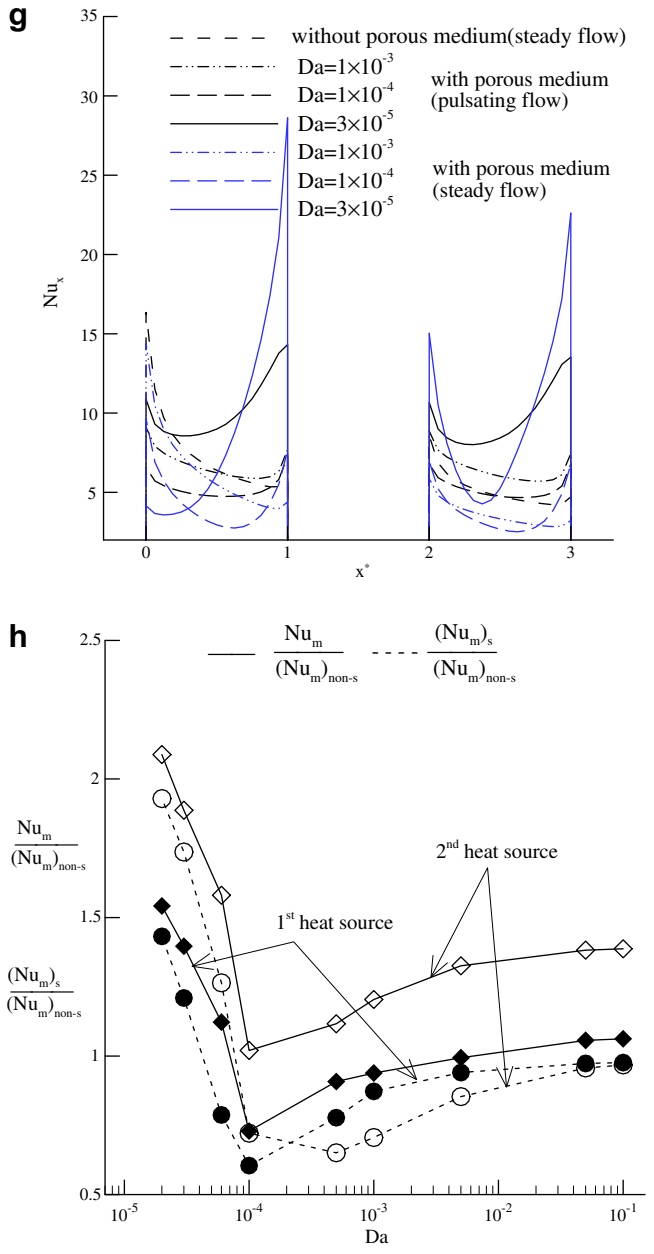

Fig. 4 (*continued*)

Nusselt number declines toward the downstream edge due to boundary layer growth. For the case of steady nonpulsating ($St = 0$) flow with porous block, at larger value of $Da(= 1 \times 10^{-3})$ Nu_x is largest at the leading edge of each heat source and then decreases rapidly to a local minimum value. Near the trailing edge of the heat source Nu_x increases slightly. The reason is that as the flow penetrates the porous block, a thermal boundary layer starts to develop at the left corner of heater. Under the blowing effect caused by porous matrix attached to heat source, the thickness of thermal boundary layer grows up quickly. Downstream the heat source face, the boundary-layer separation occurs, resulting in an increase in the convective energy transport again due to the fluid mixing. In addition, It is also seen that in Fig. 3c for the first heat source as Da decreases from ∞ to 3×10^{-5}, the one-peak type curves of local Nusselt number distribution, with which the peak value of Nu_x appears at the leading edge of heat source one, decay gradually and then transform to another one-peak one, with which the peak value of Nu_x appears at the trailing edge of heat source. For the second heat source, the one-peak type curves of local Nusselt number distribution decay gradually and then transform to two-peak type one, with which the peak value of Nu_x appears at the leading and trailing edges of the heat source and a minimum Nu_x at heater middle part where the larger and smaller vortices inside second porous block meet. This can be explained by noting that at smaller value of Da there are two thermal boundary layers starting to develop from the leading and trailing edges of each heat source. Under the clockwise and counterclockwise recirculating actions caused by porous matrix attached to source surface, both thermal-boundary-layer thickness grows up quickly along the source surface and join together at around the meeting location of the larger and smaller vortices (as shown in Fig. 3a). The heat transfer in the rear part of heat source is higher due to increased convection aided by higher velocities in the recirculation eddy. Whereas the heat transfer at around the location, where the larger and smaller vortices meet, is lower due to an almost stagnant flowfield within that region. The first source has smaller Nu_x value at the leading edge than the second source due to the impact of the core flow as it penetrates the porous block with a relative small vortex shedding at the front part of porous block and higher temperature gradient at the leading edge of heat source.

4.2. Pulsating flow

The above-stated steady and stable flow field can be destabilized by inducing pulsation, which leads to better flow mixing and further enhanced thermal transport. The influence of external forced pulsation on the flow and temperature fields is now investigated. Fig. 4a–f portraits the flow patterns and thermal fields over one pulsating cycle at a periodic-steady state with six successive phase angle of $\omega t = 0$, $\pi/3$, $2\pi/3$, π, $4\pi/3$, and $5\pi/3$ for $Re = 250$, $St = 0.8$, $A = 0.6$, $W_p^* = 1.0$, $H_p^* = 0.3$, and $\lambda_{eff} = 1.0$ at three different Darcy number $Da = 1 \times 10^{-3}$, 1×10^{-4}, and 3×10^{-5}, respectively. In Fig. 5a the u^* is plotted as a function of time at a monitoring point $(x = L_i^* + W_p^*/2, y = H_p^*/2)$ for the case with $Da = 3 \times 10^{-5}$. The x-component velocity u^* exhibits a time-asymptotic periodic-steady behavior after about 40 cycles of pulsation. Fig. 5b and c show phase diagrams of u^* vs. v^* and u^* vs. T^* at the same monitoring point. These phase diagrams display a simple closed loop, which clearly indicate that the flow and thermal fields are in a high time-periodic regime. The same well-closed loops are also found for other cases of Darcy numbers. It can be seen from Fig. 4c that for each porous block there are two recirculating cells, one before porous block on the bottom wall and the other behind porous block on the upper wall, shrinking and expanding cyclically under the action of external forcing pulsation at smaller Darcy number $Da = 3 \times 10^{-5}$. Each instantaneous flow pattern is the overall results of four competing effects – effects of penetrating, blowing, suction and boundary layer separation as mentioned earlier. This periodic alternation of flow structure contributes to the bulk mixing of fluids in the porous-block region. The interaction of recirculations, caused by both porous block and forced Pulsation, with the core flow can augment significantly the heat transfer rate from each heater face if the downstream recirculation zone on the upper wall transversely extends to more closely to the bottom wall. Fig. 4d–f shows the impact of pulsation on the thermal field. Comparison of Fig. 4d–f with Fig. 3b indicates that the thermal field under a pulsating flow presents a periodic oscillation of the thermal boundary-layer thickness. The thermal boundary-layer thickness descends during the acceleration phase of the cycle ($\omega t = 0$ to $\pi/2$ and $3\pi/2$ to 2π), and rises during the deceleration phase of the cycle ($\omega t = \pi/2$ to $3\pi/2$). This is because when the flow velocity is low, the ratio of fluid residence time over the heat source plate to the heat diffusion time is high, allowing more heat

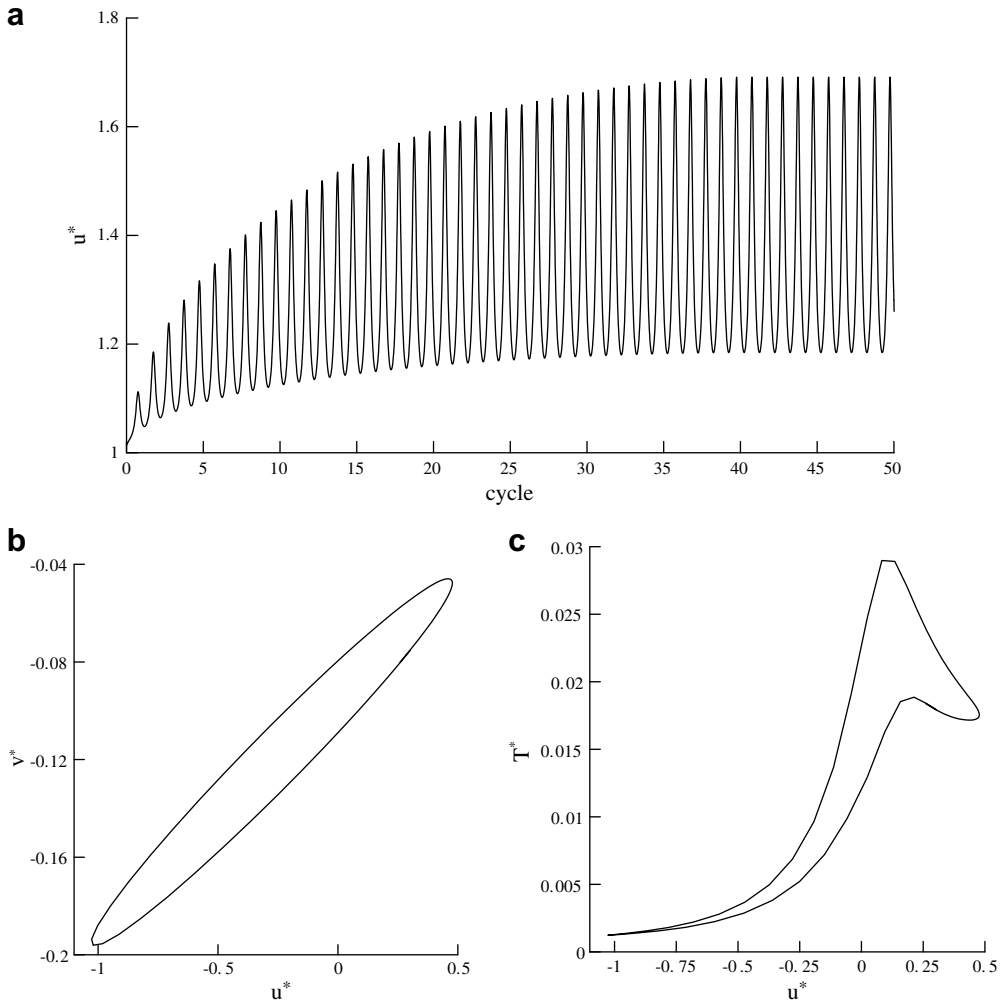

Fig. 5. A plot of the velocity u^* as a function of time (a), phase diagram of u^* vs. v^*, (b) and u^* vs. T^* (c) at $(x^*, y^*) = (L_i^* + W_p^*/2, H_p^*/2)$.

to diffuse per unit volumetric flow. This results in higher flow temperatures and less steep temperature gradient at the wall. The depth of heat penetration into the fluid increases at those times. When the flow velocity is high, decreasing that ratio leads to lower flow temperatures and greater temperature gradients. In addition, the downward transverse extension of upper recirculation zones compresses the isotherms to the bottom wall, which further increases the temperature gradients at the heater plate.

4.3. Effect of Darcy number Da

Comparison of the streamline variation in Fig. 4a–c shows that as the Darcy number increases from 3×10^{-5} to 1×10^{-3}, the distortion of streamlines becomes less pronounced, the upper recirculation behind each porous block becomes smaller and finally disappears, and the upstream recirculation before each porous block moves downstream at each time instant. This is due to the smaller bulk frictional resistance that the flow encounters in the porous region at larger values of Darcy number, which in turn accelerates the core flow through the porous block and confines the development of recirculation zones in the transverse direction. The temperature fields are affected in a similar way. Comparison of the isothermal variation in Fig. 4d–f shows that for smaller Darcy number ($Da = 3 \times 10^{-5}$), the instantaneous thickness of thermal boundary layer in the rear part of heat source becomes smaller because the transverse growth of upper recirculation zone pushes the core flow to reattach the trailing edge of heat source. This results in higher heat transport from the heat source to the core flow. Fig. 4g shows the variation of cycle-averaged local Nusselt number Nu_x with Da. For the case of pulsation flow with porous block, the variation tendency of Nu_x vs. Da is the same as that in the stated-previously case of steady nonpulsation flow with porous block. For smaller value of Da $(= 3 \times 10^{-5})$, the larger heat transfer occurring at the rear part of heat source surface is caused by the oscillating reattachment of the core flow on the heat source surface, resulting in smaller cycle-average temperature gradients.

In order to obtain an overall measure of heat transport characteristics in the present study, the influence of both flow pulsation and porous-block heat sink on the heat transfer enhancement factors $Nu_m/(Nu_m)_{\text{non-s}}$ and $(Nu_m)_s/(Nu_m)_{\text{non-s}}$, which give the cycle-space averaged Nusselt number Nu_m and steady space-averaged Nusselt number $(Nu_m)_s$ over a heat source normalized by the corresponding steady nonpulsation nonporous-block value $(Nu_m)_{\text{non-s}}$, is calculated. Fig. 4h exhibits the effect of Da on $Nu_m/(Nu_m)_{\text{non-s}}$ and $(Nu_m)_s/(Nu_m)_{\text{non-s}}$. Here, abscissa is expressed in log scale to show clearly the effect of Da in the range of $0.1{-}1 \times 10^{-5}$. It is clear from Fig. 4h that in the calculation range of Da, there exists a critical Darcy number (about $Da = 1 \times 10^{-4}$) corresponding to the smallest values of $Nu_m/(Nu_m)_{\text{non-s}}$ and $(Nu_m)_s/(Nu_m)_{\text{non-s}}$, beyond or below which both heat transfer enhancement factors increase. For the case of steady flow with porous block, the heat transfer rate is enhanced $((Nu_m)_s/(Nu_m)_{\text{non-s}} > 1)$ for the first heater at smaller

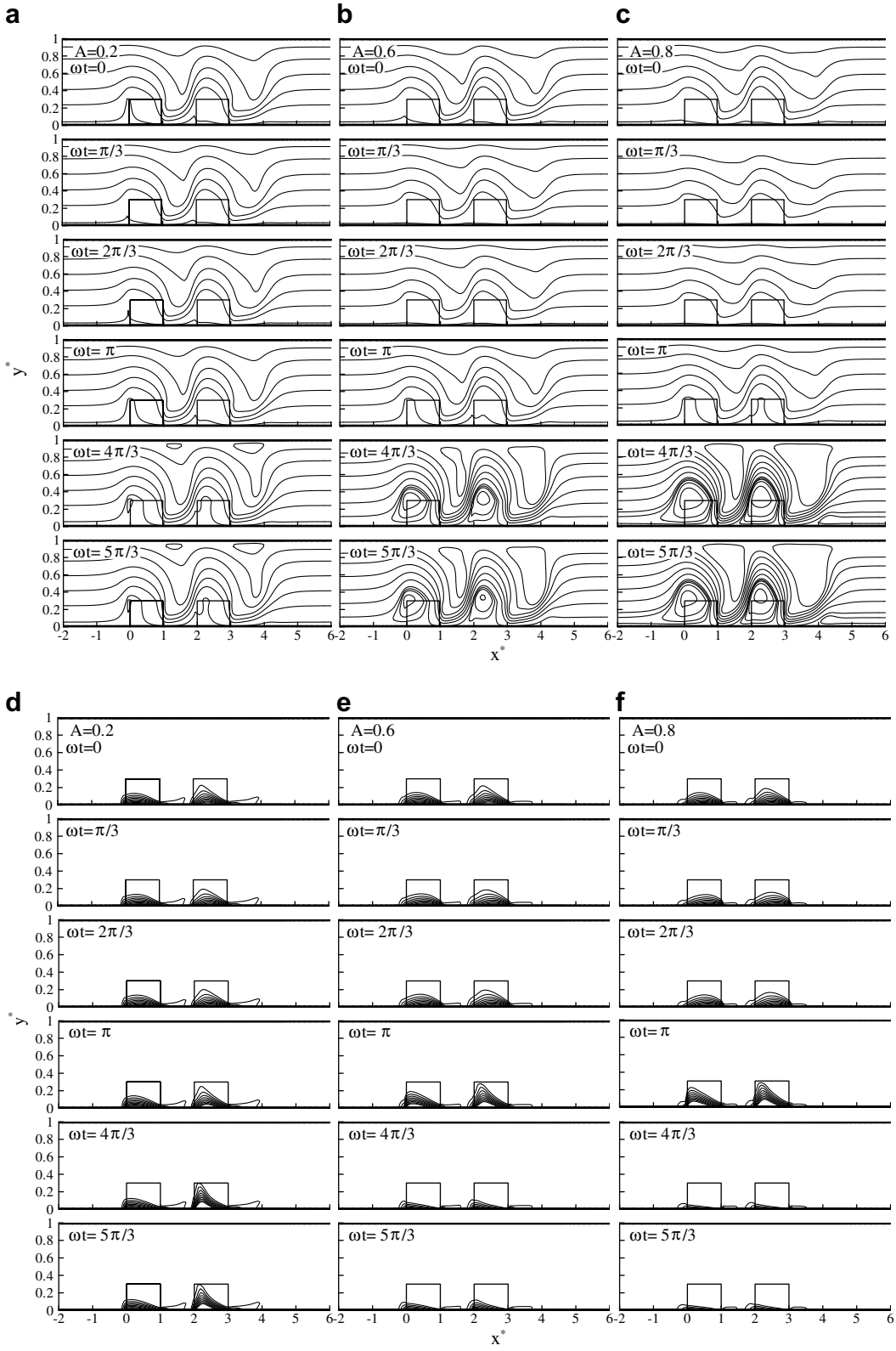

Fig. 6. Effects of the pulsating amplitude on the variations of streamlines ($\Delta\varphi^* = 0.2$ for $0 < \varphi^* < 1$) (a)–(c), isotherms ($\Delta T^* = 0.1$) (d)–(f), cycle-averaged Nusselt number (g), and heat transfer enhancement factor (h) during a periodic-steady cycle.

$Da(< 4 \times 10^{-5})$ due to increased convection aided by higher velocities in the recirculation eddy (see Fig. 3a). This enhanced effect on the second heater is better than that on the first one. For larger $Da(> 8 \times 10^{-5})$, the heat transfer rate is lessened $((Nu_m)_s/(Nu_m)_{\text{non-s}} < 1)$ for both heater due to the reduction of the mass flow rate passing over the surface of heater comparing with the case without porous block. For the case of pulsating flow with porous block, the value of pulsating heat transfer enhance-

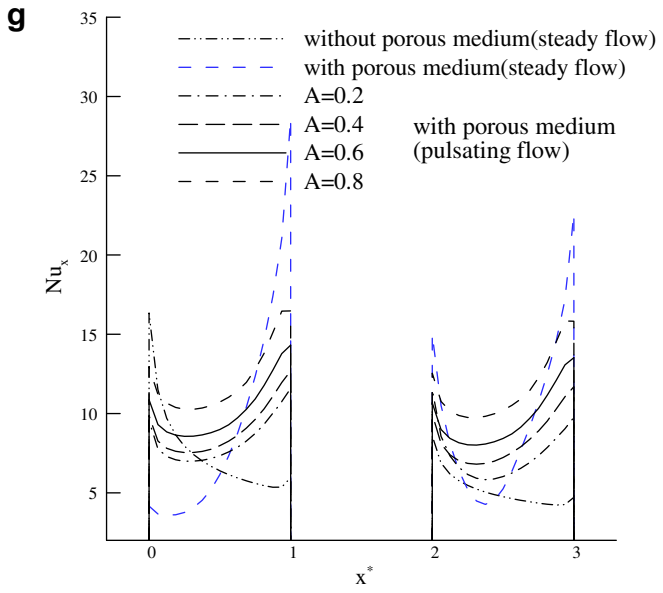

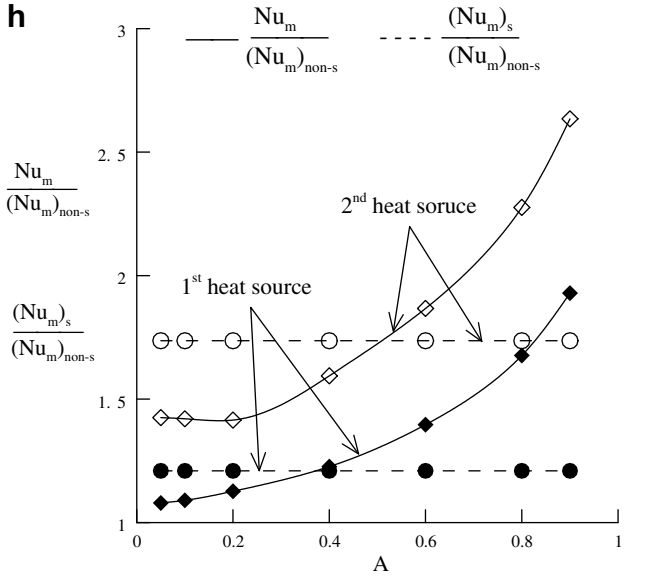

Fig. 6 (*continued*)

ment factor $Nu_m/(Nu_m)_{\text{non-s}}$ is higher than that of steady heat transfer enhancement factor $(Nu_m)_s/(Nu_m)_{\text{non-s}}$ due to the larger cycle-space averaged temperature gradient near the heat source surface. The second heater has larger value of $Nu_m/(Nu_m)_{\text{non-s}}$ than the first heater. For second heat source, when $Da = 2 \times 10^{-5}$, the cycle-space average Nusselt number of pulsating flow is about 1.20 times that of nonpulsating flow and about 2.1 times that of nonpulsating flow over nonporous-block heater. The higher cycle-space averaged Nusselt number $(Nu_m/(Nu_m)_{\text{non-s}} > 1)$ indicates that the porous-block-mounted heat source subjected to pulsating flow has a higher heat dissipation rate compared to steady flow.

4.4. Effect of the pulsating amplitude A

The influence of pulsating amplitude A on the flow and temperature fields over a periodic-steady pulsating cycle is shown in Fig. 6 for $Re = 250$, $Da = 3 \times 10^{-5}$, $St = 0.8$, $W_p^* = 1.0$, $H_p^* = 0.3$, $S_p^* = 1.0$, and $\lambda_{\text{eff}} = 1.0$ at $A = 0.2, 0.6,$ and 0.8, respectively. Based on the inlet pulsating velocity in Eq. (7), the smaller the pulsating amplitude A is, the lower the flow deceleration becomes during the flow pulsation reversal ($\omega t = \pi$ to 2π). This leads to the produce of the weaker recirculation zones due to the stronger flow momentum (as seen in Fig. 6a–c) and the larger thickness of temporal thermal boundary layer due to the reattachment of the smaller amount of core fluid to the rear part of the heat source surface (Fig. 6d–f). Fig. 6g displays the effect of A on the variation of Nu_x. It is seen that for each heat source Nu_x decreases with decreasing A due to the larger oscillation temperature gradients near the heat source surface. As expected, when A decreases, the gain in $Nu_m/(Nu_m)_{\text{non-s}}$ decreases as displayed in Fig. 6h. The second heater has a larger heat transfer enhancement factors $Nu_m/(Nu_m)_{\text{non-s}}$ and $(Nu_m)_s/(Nu_m)_{\text{non-s}}$ than the first one. In addition, when the value of A is beyond about 0.53, for both heat sources the value of pulsating heat transfer enhancement factor $Nu_m/(Nu_m)_{\text{non-s}}$ is larger than that of steady nonpulsating heat transfer enhancement factor $Nu_m/(Nu_m)_{\text{non-s}}$. The $Nu_m > (Nu_m)_s$ when $A > 0.4$ for heat source one, and when $A > 0.53$ for heat source two.

4.5. Effect of the pulsating frequency St

The effect of variations in the pulsating frequency or Strouhal number is illustrated in Fig. 7 for $Re = 250$, $Da = 3 \times 10^{-5}$, $A = 0.6$, $H_p^* = 0.3$, $W_p^* = 1.0$, $S_p^* = 1.0$, and $\lambda_{\text{eff}} = 1$, with $St = 0.4$, 1.2, and 2.0, respectively. The flow fields during a pulsating cycle with a phase angle increment of $\pi/3$ reveal that as St increases from 0.4 to 1.2, the size of upper recirculation zone behind each porous block reduces in the longitude direction (as shown in Fig. 7a and b and Fig. 4c), and the vortex upstream each porous block becomes stronger, which leads to fluid with slightly higher velocity flows through the heat source surface. As St is increased further to 2.0, the upper recirculation zone gradually disappears at each time instant. Because of a decreasing downward motion of core flow, the amount of the fluid reattaching to each heat source plate reduces. As expected, the instantaneous thickness of thermal boundary layers decreases with the increase of St from 0.4 to 1.2 (as shown in Fig. 7d and e), while slightly increases with the increase of the St from 1.2 to 2.0 (Fig. 7e and f). The effect of St on the cycle-averaged local Nusselt number distribution Nu_x is shown in Fig. 7g. It can be seen that an increase in St from 0.4 to 1.2 results in slight increase in Nu_x, until an optimal St/heat transfer rate (around $St = 1.2$) is reached and then decreases afterward. There are two reasons for this trend: the first season is that increasing Strouhal number causes heat penetrating distance into the fluid and the oscillation of this depth during a cycle to decrease, and the second is that the stronger oscillating interaction, caused by recirculations between the core flow and the heat source surface, convects more thermal energy away from the heater. The increasing rate of heat transfer is up to maximum around at $St = 1.2$, and beyond this value it decreases to a fixed value due to the reduction in the above-mentioned oscillating interaction between the core flow and the heat source surface. Again, as St increases, the gain in $Nu_m/(Nu_m)_{\text{non-s}}$ gradually increases to a maximum $Nu_m/(Nu_m)_{\text{non-s}} = 1.41$ for the first heater, and $Nu_m/(Nu_m)_{\text{non-s}} = 1.91$ for the second heater around $St \sim 1.2$, as displayed in Fig. 7h, and then decreases to a fixed value. The heat transfer enhancement factor is insensitive to the changes in the pulsating frequency when $St > 1.6$. For the first heater, the pulsating heat transfer enhancement factor $Nu_m/(Nu_m)_{\text{non-s}}$ is always larger than steady heat transfer enhancement factor $(Nu_m)_s/(Nu_m)_{\text{non-s}}$. For the second heater, $Nu_m/(Nu_m)_{\text{non-s}} > (Nu_m)_s/(Nu_m)_{\text{non-s}}$ only when $St > 0.6$. Also, the heater two has a larger heat transfer enhancement factors $Nu_m/(Nu_m)_{\text{non-s}}$ and $(Nu_m)_s/(Nu_m)_{\text{non-s}}$ than heater one in the estimated range of St.

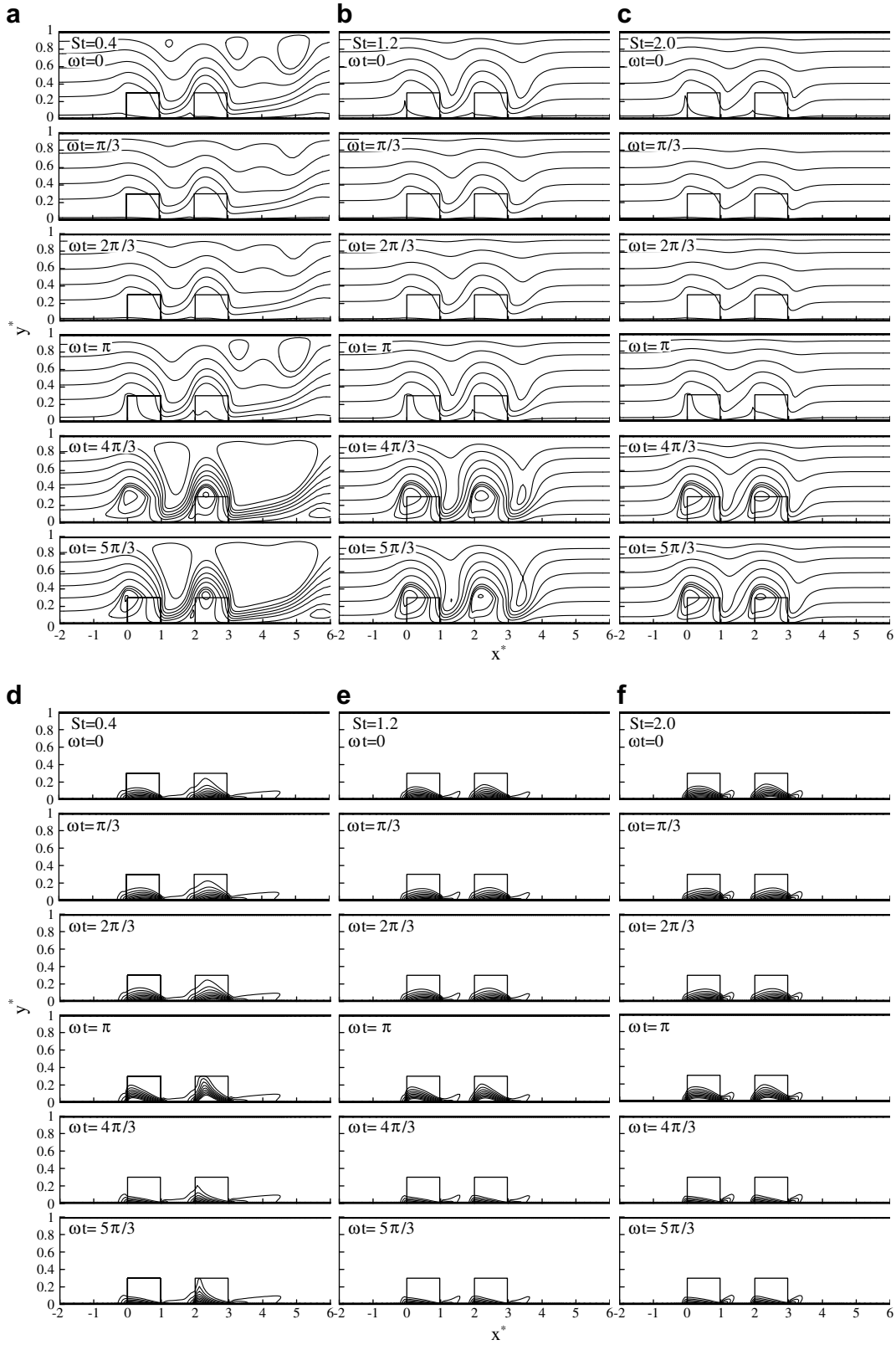

Fig. 7. Effects of the Strouhal number on the variations of streamlines ($\Delta\varphi^* = 0.2$ for $0 < \varphi^* < 1$) (a)–(c), isotherms ($\Delta T^* = 0.1$) (d)–(f), cycle-averaged Nusselt number (g), and heat transfer enhancement factor (h) during a periodic-steady cycle.

4.6. Effect of the porous blockage ratio H_p^*

Fig. 8 presents the changes in Nu_x, $Nu_m/(Nu_m)_{\text{non-s}}$ and $(Nu_m)_s/(Nu_m)_{\text{non-s}}$ as the porous block height H_p^* increases from 0.1 to 0.4 for $Re = 250$, $Da = 3 \times 10^{-5}$, $A = 0.6$, $St = 0.8$, $W_p^* = 1.0$, $S_p^* = 1.0$, and $\lambda_{\text{eff}} = 1$. As can be seen in Fig. 8a–c that the distortions for streamlines and isotherms (not shown) become more conspicuous in each time as the block height increases from

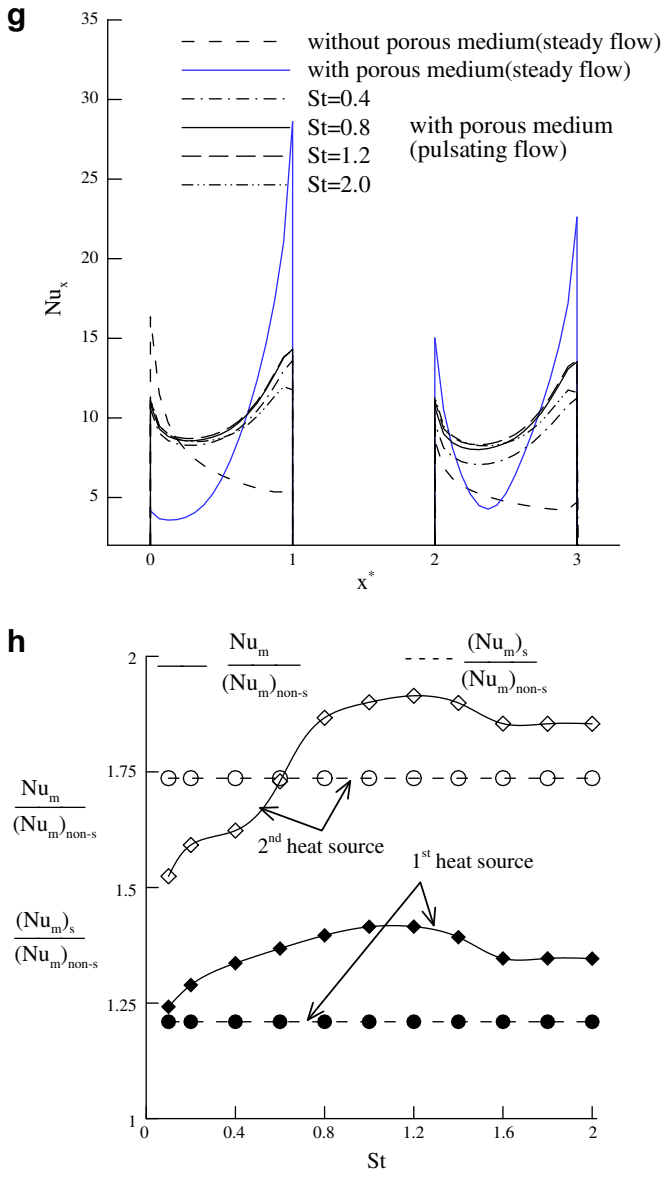

Fig. 7 (*continued*)

0.2 to 0.4. The transverse size and strength of the upstream and downstream recirculation zones for each porous block increase with increasing H_p^*. This is due to the relative increase in the height of the porous block, which in turn offers a higher degree of obstruction and a larger blowing action to the flow for larger values of H_p^*. This leads to a stronger suction effect caused by the pressure drop behind the porous block resulting in a stronger reattached flow. Meanwhile, the thermal field exhibits smaller instantaneous thermal-boundary-layer thickness at each time instant for the larger H_p^*. As expected, Nu_x increases with increasing H_p^* from 0.15 to 0.4, as shown in Fig. 8d, due to the existing of larger temperature gradient near the heater surface for the larger H_p^*. Therefore, the gain in $Nu_m/(Nu_m)_{non\text{-}s}$ is more substantial for larger H_p^*, as shown in Fig. 8e. Whereas as H_p^* decreases from 0.15 to 0.1, Nu_x increases inversely due to the quite small blowing effect resulting in larger transient temperature gradient near the heater surface. For the steady nonpulsating flow, the increase trend of heat transfer enhancement factor $(Nu_m)_s/(Nu_m)_{non\text{-}s}$ vs H_p^* is steeper than that in the pulsating-flow case, especially in H_p^* from 0.2 to 0.4. In other words, when the value of H_p^* is less than 0.3, the heat transfer enhancement factor of each heater $Nu_m/(Nu_m)_{non\text{-}s} > (Nu_m)_s/(Nu_m)_{non\text{-}s}$, while the value of H_p^* is larger than 0.3, $Nu_m/(Nu_m)_{non\text{-}s} < (Nu_m)_s/(Nu_m)_{non\text{-}s}$. This is due to the larger cycle-space average temperature gradient existing in heater surface for the steady flow than for the pulsating flow as H_p^* increases from 0.3 to 0.4. Again, the heat source two is better in the enhanced heat transfer than heat source one in the estimated range of H_p^*.

4.7. The variations of cycle-average local surface temperature distribution

The local surface temperature of the heater is more important than the averaged surface temperature in the application of electronic cooling [27]. Fig. 9 shows the variations of cycle-average local temperature distribution along heat source surfaces for various values of Da, A, St, and H_p^*. As seen in Fig. 9, for the pure steady-flow case, the surface temperature of heaters increases along flow direction and approaches a constant maximum value when the flow approaches the thermally developed region. However, for the steady-flow or pulsating-flow case with porous block, the heater surface temperature distribution curves are of convex shape due to the boundary layer reattaching on the rear parts of heaters. The maximum temperature point occurs at the center section of each heater surface, where the thickness of the thermal boundary layer approaches to maximum.

It can be seen from Fig. 9a (at $Re = 250$, $St = 0.8$, $A = 0.6$, $W_p^* = 1.0$, $H_p^* = 0.3$, and $\lambda_{eff} = 1.0$) that for steady flow with porous block the maximum temperature moves from the rear part of heater surface to the front part of heater surface as Da decreases from 1×10^{-3} to 3×10^{-5}. The maximum temperature occurs at $Da = 1 \times 10^{-4}$. Below and above this critical value, the maximum temperature becomes fewer. At $Da = 3 \times 10^{-5}$ the maximum temperature of heater two is smaller than that of heater one due to larger convection heat transfer aided by the stronger downstream recirculation eddy (see Fig. 3a). Comparison of the cycle-average local surface temperature distribution T_x^* of pulsating-flow case with steady-flow case in Fig. 9a indicates that the cycle-average local surface temperature distribution for pulsating-flow case with porous block is more uniform than that for steady-flow case with or without porous block. Namely, the temperature difference between the maximum and minimum temperatures on the surface of heat sources for pure steady-flow case is higher than that for pulsating-flow case with porous block. In addition, the maximum temperatures T_x^* at the heater surface is smaller for pulsating-flow case with porous block than for steady-flow case with or without porous block. This is because the larger cycle-space averaged temperature gradient near the heater surface leads to more heat removal, which low the global surface temperature level.

The local surface temperature distribution uniformity of each heater increases as pulsating amplitude A (at $Re = 250$, $Da = 3 \times 10^{-5}$, $St = 0.8$, $W_p^* = 1.0$, $H_p^* = 0.3$, $S_p^* = 1.0$, and $\lambda_{eff} = 1.0$) or blockage ratio number H_p^* (at $Re = 250$, $Da = 3 \times 10^{-5}$, $A = 0.6$, $St = 0.8$, $W_p^* = 1.0$, $S_p^* = 1.0$, and $\lambda_{eff} = 1$) increases, as seen in Fig. 9b and d. The reason is due to smaller cycle-average thermal-boundary-layer thickness as discussed previously. As seen in Fig. 9c, the surface temperature distribution uniformity of each heater slightly (for $Re = 250$, $Da = 3 \times 10^{-5}$, $A = 0.6$, $H_p^* = 0.3$, $W_p^* = 1.0$, $S_p^* = 1.0$, and $\lambda_{eff} = 1$) increases as St increases from 0.4 to 1.2, whereas it decreases to a fixed uniform distribution as St increases from 1.2 to 20.

4.8. Pressure drop calculation

When using both inducing pulsation and porous material for augmenting heat transfer, an important factor to consider is the penalty arising from increased pressure drop. In the stream func-

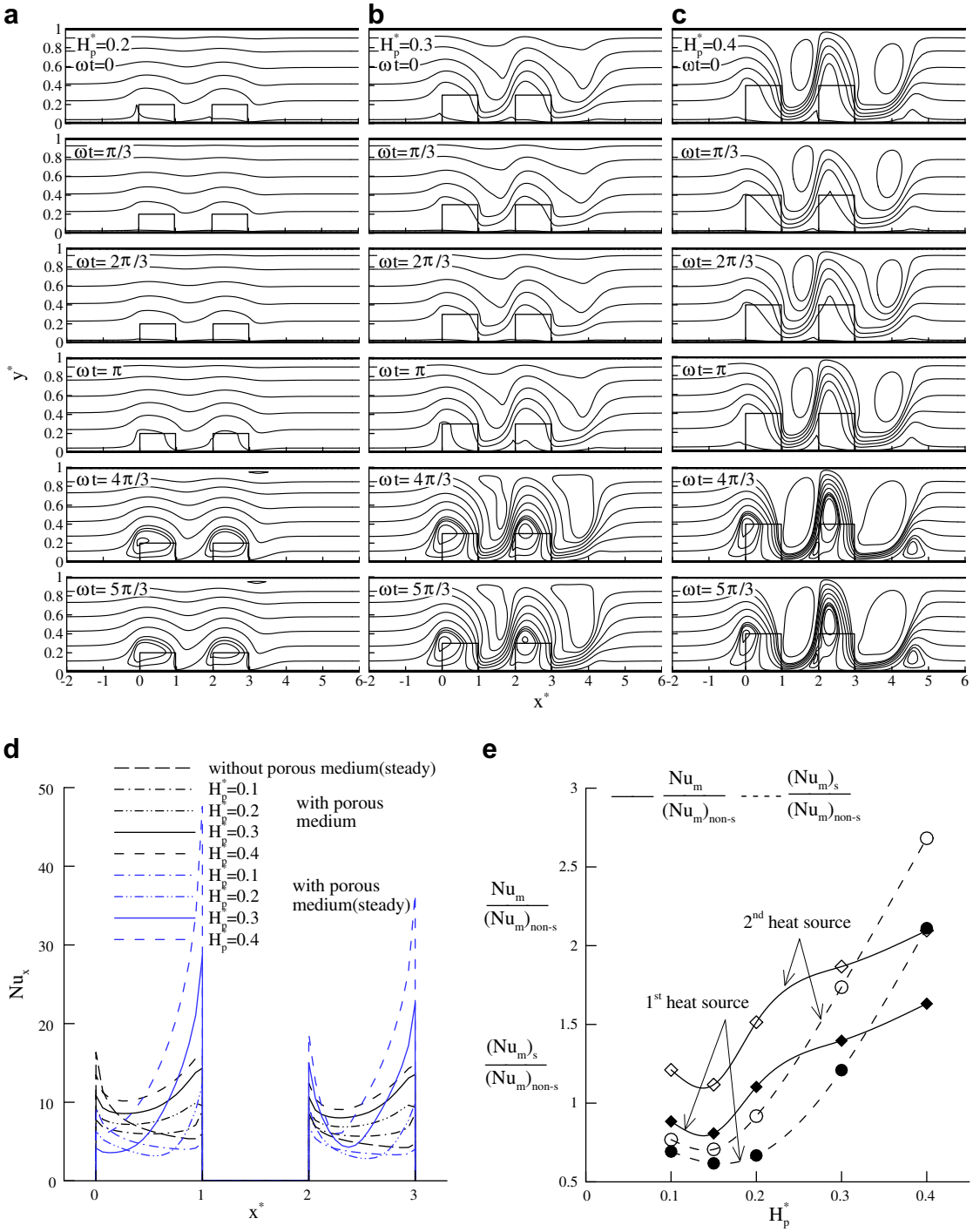

Fig. 8. Effects of the porous blockage ratio H_p^* on the variations of streamlines ($\Delta\varphi^* = 0.2$ for $0 < \varphi^* < 1$) (a)–(c), cycle-averaged Nusselt number (d), and heat transfer enhancement factor (e) during a periodic-steady cycle.

tion-vorticity formulation, the pressure field is eliminated in obtaining the solution. However, the pressure field can be recovered from the converged stream function and vorticity fields. This is done by integrating the pressure gradient along the upper channel wall. The temporal pressure gradient in a periodic steady state is derived from the unsteady momentum equation using the no-slip boundary conditions on the solid wall. The total temporal pressure drop ΔP^* along the upper channel wall is then obtained from

$$\Delta P^* = \int_0^{L_t^*} \left.\frac{\partial P^*}{\partial x^*}\right|_{y^*=1} dx^* = -\int_0^{L_t^*} \left[\frac{\partial u^*}{\partial t^*} + \frac{1}{Re}\frac{\partial \xi^*}{\partial y^*}\right]_{y^*=1} dx^*. \quad (24)$$

The corresponding steady nonpulsating nonporous-block pressure drop $(\Delta P^*)_{non\text{-}s}$ is

$$(\Delta P^*)_{non\text{-}s} = \int_0^{L_t^*} \left.\frac{\partial P^*}{\partial x^*}\right|_{y^*=1} dx^* = -\int_0^{L_t^*} \frac{1}{Re}\left.\frac{\partial \xi^*}{\partial y^*}\right|_{y^*=1} dx^*, \quad (25)$$

where pressure P^* is nondimensionalized with respect to ρu_o^2. The effects of Da, A, St, and H_p^* on the temporal pressure drop factor $\Delta P^*/(\Delta P^*)_{non\text{-}s}$, which gives the overall pressure drop throughout the entire channel length, normalized by the corresponding steady nonpulsating nonporous-block value $(\Delta P^*)_{non\text{-}s}$, is presented in Fig. 10, respectively. In Fig. 10(a), the amplitude of the temporal

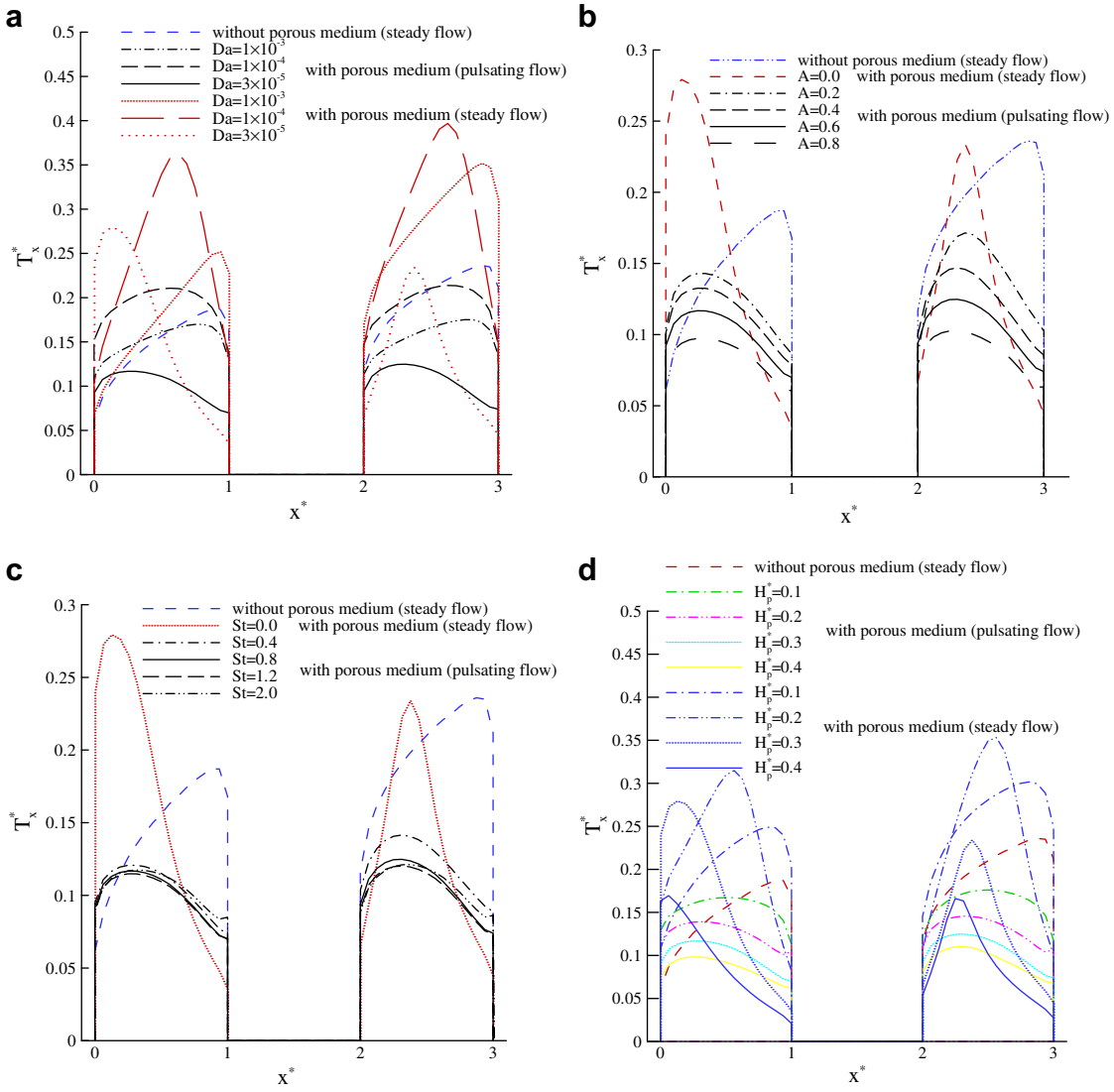

Fig. 9. The variations of cycle-average local temperature distribution along heat source surfaces for various values of (a) *Da*, (b) *A*, (c) *St*, and (d) H_p^*.

pressure drop factor is less affected by a change in *St* (at $Re = 250$, $Da = 3 \times 10^{-5}$, $A = 0.6$, $H_p^* = 0.3$, $W_p^* = 1.0$, and $S_p^* = 1.0$). However, the magnitude of $\Delta P^*/(\Delta P^*)_{\text{non-s}}$ increases substantially as *A* (at $Re = 250$, $Da = 3 \times 10^{-5}$, $St = 0.8$, $W_p^* = 1.0$, $H_p^* = 0.3$, $S_p^* = 1.0$) or H_p^* (at $Re = 250$, $Da = 3 \times 10^{-5}$, $A = 0.6$, $St = 0.8$, $W_p^* = 1.0$, and $S_p^* = 1.0$) increases and or as *Da* (at $Re = 250$, $St = 0.8$, $A = 0.6$, $W_p^* = 1.0$, $H_p^* = 0.3$, and $S_p^* = 1.0$) decreases, as seen in Fig. 10b–d. The reason is that as the flow approaches the smaller passage formed by the porous block and the upper surface of the channel, the fluid starts to accelerate, resulting in an increase in the pressure drop. The temporal pressure recovery behind each porous block is not complete due to the pressure loss in the recirculation zones. An increase inH_p^* or decrease in *Da* provides larger bulk frictional resistance that the flow encounters in the channel, resulting in a significant increase in variations of temporal pressure drop. An increase in *A* also leads to a larger pressure loss due to the formation of larger recirculating zones in the channel as stated previously. Therefore, the required pumping power to maintain a pulsating flow increases as pulsation amplitude, Darcy number and porous blockage ratio. The phase lead of temporal pressure gradient $\Delta P^*/(\Delta P^*)_{\text{non-s}}$ over the inlet pulsating velocity for all cases studied here is around $\pi/2$. This indicated that the flow pulsation considered in this study is in a higher frequency regime, compared to the oscillating flow inside a smooth duct [24]. In this classical oscillating flow, the phase leads of pressure drop over the inlet velocity approaches $\pi/2$ from zero as ω increases.

5. Conclusion

In this study, the flow and thermal characteristics of pulsating flow through a channel with two porous-block-mounted heat sources in tandem are investigated. Findings indicate that for the case of nonpulsating steady flow the heat transfer rate from strip heaters could be enhanced by fiber porous-block heat sink, which depends on the consolidated result of four interrelated effects caused by porous block: penetrating, blowing, suction and boundary layer separation. For the case of pulsating flow, the steady and stable flow field is substantially destabilized by external pulsation and exhibits a cyclic expanding and shrinking alteration of the vortex structure. The phase diagrams also show that this unsteady pulsating flow is highly periodic and well organized. The temperature field is significantly affected by such increased large-scale flow mixing and presents a periodic oscillation of the thermal boundary-layer thickness near the heater surface. The cycle-average local surface temperature distribution of each heater for

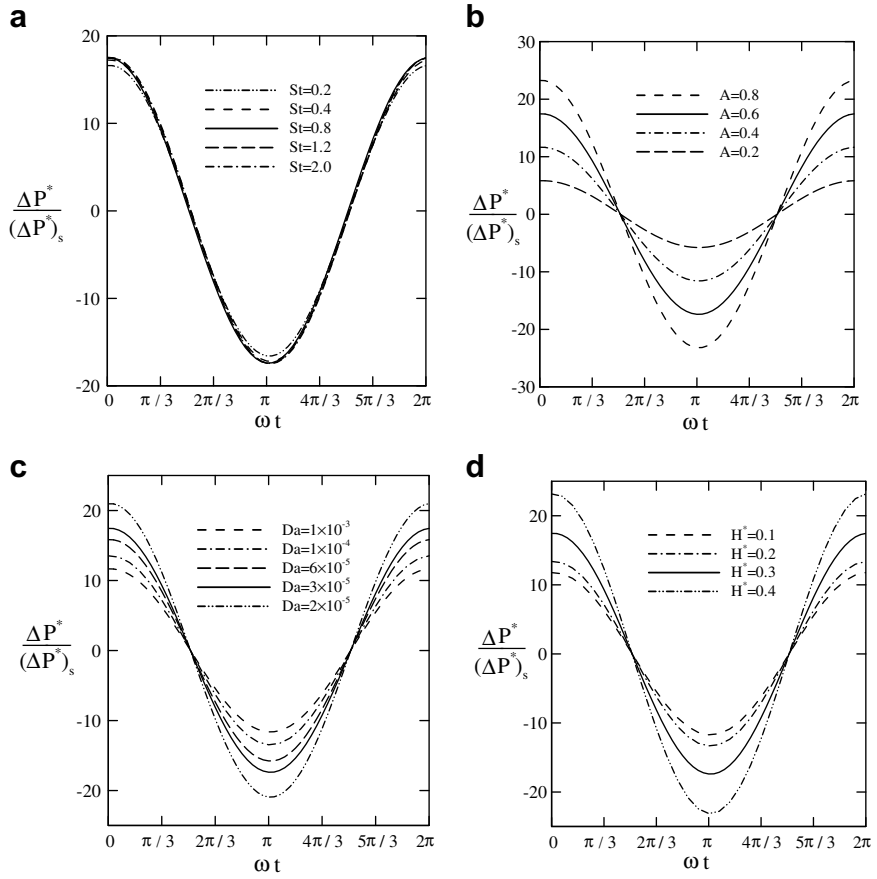

Fig. 10. The variations of temporal pressure drop factor along the upper plate for various values of (a) *Da*, (b) *A*, (c) *St*, and (d) H_p^*.

pulsating-flow case with porous block is more uniform than that for pure steady-flow case. It is shown the heat transfer enhancement factor $Nu_m/(Nu_m)_{\text{non-s}}$ of the heaters increases with the pulsating amplitude. However, the effects of Darcy number, Strouhal number and porous blockage ratio are not straightforward. There exists a critical value for which the heat transfer enhancement factor is minimum (for Darcy and blockage ratio numbers) or maximum (for Strouhal number). Below and above this critical value, the heat transfer enhancement factor drops off or goes up. Under specific choices of descriptive parameters, the value of pulsating heat transfer enhancement factor $Nu_m/(Nu_m)_{\text{non-s}}$ is larger than that of steady heat transfer enhancement factor $(Nu_m)_s/(Nu_m)_{\text{non-s}}$.

The results of this investigation clearly demonstrate that the strip heat source with fiber porous-block heat sink subjected to forced pulsating channel is an effective method for cooling electronic devices. However, one must consider a tolerance limit in view of increased pressure drop to determine the optimal amplitude of external pulsation according to the porous blockage ratio and porous material.

Acknowledgements

This work was supported by the ROC National Science Council and the ROC Ministry of Economic Affairs, Bureau of Energy under Contracts NSC 93-2212-E-027-012 and 97-D0137-3.

References

[1] M. Mahalingam, H. Berg, Thermal trend in component level packaging, Int. J. Hybrid Microelectron. 7 (1984) 1–9.
[2] R. Simon, Thermal management of electronic packages, Solid State Technol. 26 (1983) 131–137.
[3] J.C.Y. Koh, R. Colony, Analysis of cooling effectiveness for porous material in a coolant passage, ASME J. Heat Transfer 96 (1974) 324–330.
[4] M. Kaviany, Laminar flow through a porous channel bounded by isothermal parallel plate, Int. J. Heat Mass Transfer 28 (1985) 851–858.
[5] P.C. Huang, K. Vafai, Analysis of forced convection enhancement in a parallel plate using porous blocks, AIAA J. Thermophys. Heat Transfer 18 (1994) 563–573.
[6] D. Angirasa, Forced convective heat transfer in metallic fibrous materials, ASME J. Heat Transfer 124 (2002) 739–745.
[7] H.A. Hadim, A. Bethancourt, Numerical study of forced convection in a partially porous channel with discrete heat sources, ASME J. Heat Transfer 8 (1995) 465–472.
[8] D. Angirasa, G.P. Peterson, Forced convection heat transfer augmentation in a channel with a localized heat source using metal fibrous material, ASME J. Electron. Packaging 121 (1999) 1–7.
[9] W.S. Fu, H.C. Huang, W.Y. Liou, Thermal enhancement in laminar channel flow with a porous block, Int. J. Heat Mass Transfer 39 (1996) 2165–2175.
[10] P.C. Huang, C.F. Yang, J.J. Hwang, M.T. Chiu, Enhancement of forced-convection cooling of multiple heated blocks in a channel using porous covers, Int. J. Heat Mass Transfer 48 (2005) 647–664.
[11] S. Uchida, The pulsating viscous flow superimposed on the steady laminar motion of incompressible fluids in a Circular pipe, ZAMP VII (1956) 403–422.
[12] R. Siegel, M. Perlmutter, Heat transfer for pulsating laminar duct flow, ASME J. Heat Transfer 84 (1962) 111–123.
[13] S.Y. Kim, B.H. Kang, J.M. Hyun, Heat transfer in the thermally developing region of a pulsating channel flow, Int. J. Heat Mass Transfer 36 (1993) 4257–4266.
[14] S.Y. Kim, B.H. Kang, J.M. Hyun, Heat transfer from pulsating flow in channel filled with porous media, Int. J. Heat Mass Transfer 37 (1994) 2025–2033.
[15] J.M. Khodadadi, Oscillatory fluid flow through a porous medium channel bounded by two impermeable parallel plates, ASME J. Fluid Eng. 113 (1991) 509–511.
[16] J.W. Paek, B.H. Kang, J.M. Hyun, Transient cool-down of a porous medium in pulsating flow, Int. J. Heat Mass Transfer 42 (1999) 3523–3527.
[17] H.L. Fu, K.C. Leong, X.Y. Huang, C.Y. Liu, An experimental study of heat transfer of a porous channel subjected to oscillating flow, ASME J. Heat Transfer 123 (2001) 163–170.
[18] K.C. Leong, L.W. Jin, An experimental study of heat transfer in oscillating flow through a channel filled with an aluminum foam, Int. J. Heat Mass Transfer 48 (2005) 243–253.

[19] Z. Guo, S.Y. Kim, H.Y. Sung, Pulsating flow and heat transfer in a pipe partially filled with a porous medium, Int. J. Heat Mass Transfer 40 (1997) 4209–4218.
[20] M.L. Hunt, C.L. Tien, Effects of thermal dispersion on forced convection in fibrous media, Int. J. Heat Mass Transfer 31 (1988) 301–310.
[21] A. Amiri, K. Vafai, Transient analysis of incompressible flow through a packed bed, Int. J. Heat Mass Transfer 41 (1998) 4259–4279.
[22] J. Adams, J. Ortega, A multicolor SOR method for parallel computation, Proc. Int. Conf. on Parallel Procession (1982) 53–56.
[23] S.W. Patanker, Numerical Heat Transfer and Fluid Flow, McGraw-Hill, New York, 1980. pp. 79–138 (Chapters 5 and 6).
[24] H. Schlichting, Boundary-Layer Theory, McGraw-Hill, New York, 1979.
[25] H.J. Sung, S.Y. Kim, J.M. Hyun, Forced convection from an isolated heat source in a channel with porous medium, Int. J. Heat Fluid Flow 16 (1995) 527–535.
[26] S.Y. Kim, B.H. Kang, Forced convection heat transfer from two heated blocks in pulsating channel flow, Int. J. Heat Mass Flow 41 (1998) 625–634.
[27] G. Hwang, C. Chao, Heat transfer measurement and analysis for sintered porous channels, ASME J. Heat Transfer 116 (1994) 456–464.